Sensors & Actuators: B. Chemical 370 (2022) 132427

Contents lists available at ScienceDirect

Sensors and Actuators: B. Chemical

journal homepage: www.elsevier.com/locate/snb

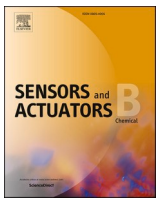

Enhanced susceptibility of SARS-CoV-2 spike RBD protein assay targeted by cellular receptors ACE2 and CD147: Multivariate data analysis of multisine impedimetric response

Mateusz Brodowski [a,b], Mattia Pierpaoli [b], Monika Janik [b,c], Marcin Kowalski [d], Mateusz Ficek [b], Pawel Slepski [e], Bartosz Trzaskowski [f], Greg Swain [g], Jacek Ryl [a,*], Robert Bogdanowicz [b,*]

[a] Division of Electrochemistry and Surface Physical Chemistry, Institute of Nanotechnology and Materials Engineering, Gdańsk University of Technology, 11/12 Narutowicza, 80-233 Gdansk, Poland
[b] Department of Metrology and Optoelectronics, Gdańsk University of Technology, 11/12 Narutowicza, 80-233 Gdansk, Poland
[c] Faculty of Electronics and Information Technology, Warsaw University of Technology, Koszykowa 75, 00-662 Warsaw, Poland
[d] Institute of Biotechnology and Molecular Medicine, 25 Kampinoska, 80-180 Gdańsk, Poland
[e] Faculty of Chemistry, Gdańsk University of Technology, 11/12 Narutowicza, 80-233 Gdansk, Poland
[f] Centre of New Technologies, University of Warsaw, 2c Banach St, 02-097 Warsaw, Poland
[g] Department of Chemistry, Michigan State University, 578 S. Shaw Lane, East Lansing, MI 48824-1322, United States

ARTICLE INFO

Keywords:
SARS-CoV-2
Immunosensor
Impedance monitoring
ACE2
CD147
Multivariate statistical analysis

ABSTRACT

Severe acute respiratory syndrome coronavirus 2 (SARS-CoV-2) enters the cells through the binding of spike protein to the host cell surface-expressing angiotensin-converting enzyme 2 (ACE2) or by endocytosis mediated by extracellular matrix metalloproteinase inducer (CD147). We present extended statistical studies of the multisine dynamic electrochemical impedance spectroscopy (DEIS) revealing interactions between Spike RBD and cellular receptors ACE2 and CD147, and a reference anti-RBD antibody (IgG2B) based on a functionalised boron-doped diamond (BDD) electrode. The DEIS was supported by a multivariate data analysis of a SARS-CoV-2 Spike RBD assay and cross-correlated with the atomic-level information revealed by molecular dynamics simulations. This approach allowed us to study and detect subtle changes in the electrical properties responsible for the susceptibility of cellular receptors to SARS-CoV-2, revealing their interactions. Changes in electrical homogeneity in the function of the RBD concentration led to the conclusion that the ACE2 receptor delivers the most homogeneous surface, delivered by the high electrostatic potential of the relevant docking regions. For higher RBD concentrations, the differences in electrical homogeneity between electrodes with different receptors vanish. Collectively, this study reveals interdependent virus entry pathways involving separately ACE2, CD147, and spike protein, as assessed using a biosensing platform for the rapid screening of cellular interactions (i.e. testing various mutations of SARS-CoV-2 or screening of therapeutic drugs).

1. Introduction

The worldwide SARS-CoV-2 pandemic triggered an urgent need for effective sensing and therapeutic solutions to efficiently detect, prevent, and treat the resulting COVID-19 disease. Since the beginning of 2020, rapid progress has been made on understanding the molecular basis of viral infection, therefore inhibiting the initial, crucial steps of viral-host cell recognition. These, in turn, have been identified as promising strategies for therapeutic solutions/treatment/intervention [1].

SARS-CoV-2 is an enveloped, single-stranded RNA virus belonging to the family of *Coronaviridae*. The genome of the virus encodes four major structural proteins, namely spike (S), envelope, membrane, and nucleocapsid [2,3]. Among them, protein S plays an essential role in viral attachment, fusion, entry, and transmission [4]. Protein S comprises an N-terminal S1 subunit responsible mainly for virus-receptor binding and a C-terminal S2 subunit responsible for virus-cell membrane fusion. S1 can be further divided into an N-terminal domain (NTD) and a receptor-binding domain (RBD), where RBD interaction with cellular receptors is essential for SARS-CoV-2 infectivity [5].

To gain entry into human cells, SARS-CoV2 uses primarily the

* Corresponding authors.
E-mail addresses: jacek.ryl@pg.edu.pl (J. Ryl), rbogdan@eti.pg.edu.pl (R. Bogdanowicz).

https://doi.org/10.1016/j.snb.2022.132427
Received 14 April 2022; Received in revised form 20 July 2022; Accepted 24 July 2022
Available online 27 July 2022

metallocarboxyl peptidase angiotensin receptor (ACE2) [6,7]. ACE2 is a cellular membrane-bound, zinc-containing carboxypeptidase. This type I single-pass membrane protein is predominantly expressed in the cardiovascular system and kidneys, where it plays a role in maintaining water electrolyte homeostasis [8]. However, it has been shown that immune cells can also be potentially targeted by SARS-CoV-2. ACE2 is rarely expressed in immune cells; therefore, it was assumed that there might be other receptors for virus entry in different cell types. Indeed, other recently reported host cell components (co-factors) have also been suggested to play a vital role for viral attachment or entry, such as GRP78 or CD147 (also known as EMMPRIN, or Basigin) [9,10]. Among them, CD147 is a type I integral membrane glycoprotein that belongs to the immunoglobulin (Ig) superfamily. It is expressed in a wide variety of cells and plays the role of a transmembrane receptor that interacts with several extracellular and intracellular partners and forms transmembrane supramolecular complexes. It participates mainly in tumour development, plasmodium invasion, and bacterial/viral infections [11, 12]. Moreover, the studied receptors are regulated by age, underlying chronic inflammation, or comorbidities, therefore potentially predisposing patients to SARS-CoV-2 infection [13]. Thus, a deep understanding and quantitative analysis of these receptors-target interactions are essential for detecting the virus itself, but more importantly, for fighting emerging SARS-CoV-2 variants, which provides a platform for testing attractive/promising therapeutic strategies.

Nowadays, the reverse transcription-polymerase chain reaction (RT-PCR)-based test for viral RNA detection is considered the standard gold method for the diagnosis of COVID-19 [14]. However, the price of a single test and the time it takes have forced the entire scientific community to research and develop new ways to quickly and cheaply detect SARS-Cov-2 [15,16]. Recently, impedimetric [17–20] and resistive [21, 22] biosensors were considered as selective and rapid platforms for the determination of the SARS-CoV-2 spike S1 protein. Despite their advantages (high sensitivity or selectivity), these methods have important limitations. Measurements are usually made at a predetermined potential at which the presence of SARS-CoV-2 indicates a change in resistance. This potential is dependent on multiple factors, such the electrode preparation methodology, the type and concentration of the electrolyte, the dynamics of the phenomena occurring at the electrode, or even the amplitude of the AC signal perturbation [23].

Multisine impedimetric probing based on Dynamic Electrochemical Impedance Spectroscopy (DEIS) is one of the techniques that has received growing attention in electrochemical sensing in the last few years, but has not been manifested in SARS-CoV-2 detection. This electrochemical method utilises a multifrequency perturbation signal with all of the elementary frequencies superimposed and applied simultaneously in the studied system. The excitation signal is generated continuously during the experiment, and the registered changes in potential and current are sequenced into appropriate portions and transformed using Fourier transform. Such a process produces a series of instantaneous impedance spectra, thus offering the opportunity to investigate non-stationary processes [24,25]. For example, the impedimetric (resistive or capacitive) response may be studied in real time upon specific or non-specific binding occurring at the electrode surface. Importantly, DEIS provides a unique opportunity for rapid monitoring as a function of an independent variable, such as time, polarisation potential, or analyte concentration. The approach is particularly advantageous in studying complex analyte interactions during flow injection analysis [26] and at charged-up electrode surfaces [27]. Unlike classic impedance spectroscopy measurement, in DEIS the system stationary condition does not need to be fulfilled. Thus, the approach is particularly advantageous if the initial electrode conditions are not well established, which forms the primary challenge towards high the uncertainty of macromolecular detection. The initial electrode state is highly dependent on internal (i.e., electrode polycrystallinity, functionalisation thickness, and density) and external (i.e. surface contamination, local pH or oxygen concentration changes) factors.

This work presents a novel alternative approach to studying the SARS-CoV-2 Spike RBD complex interaction by multisine impedimetric probing at a functionalised boron-doped diamond (BDD) sensor, using various cellular receptors, namely ACE2, CD147, and a monoclonal anti-RBD antibody (IgG2B) as the reference. Identification of patterns in the impedimetric response and resulting from the unique molecular recognition mechanisms by all of the studied receptors may be used in two ways: (i) recognition of optimal detection conditions (i.e. frequency range and polarisation), and (ii) in the future creating a multi-receptor sensing platform with substantially improved detection selectivity and specificity. To achieve our goal, a statistical and multivariate data analysis of the multisine DEIS impedimetric monitoring data was performed for the first time. This allowed us to study and detect subtle changes of the electric properties at the charged, biofunctionalised electrode surface, including changes in spatial homogeneity or surface blockage. The proposed approach makes it possible to assess the optimised polarisation conditions, efficiently differentiating results of the electric parameters between the analyte and blank samples. The obtained results expand the understanding of the frequency- and polarisation-dependent electrochemical characteristics of the sensors. Furthermore, studies allows for a rapid screening of physiological factors influencing cellular interactions, mutations of SARS-CoV-2, or investigations of future therapeutic drugs.

2. Experimental

2.1. Reagents

1-Ethyl-3-(3-dimethylaminopropyl) carbodiimide (EDC), N-Hydroxysuccinimide (NHS), nickel (II) chloride, Nα,Nα-Bis(carboxymethyl)-L-lysine hydrate (NTA), bovine serum albumin (BSA), tetraethylammonium tetrafluoroborate ($Et_4N(BF_4)$), tetrafluoroboric acid (48 wt% water), sodium bicarbonate and sodium carbonate were purchased from Sigma Aldrich. Potassium ferric hexacyanoferrate, potassium hexacyanoferrate(ii) trihydrate, sodium nitrate and methanol were purchased from Chempur. Avantor Performance Materials delivered acetonitrile and diethyl ether. P-aminobenzoic acid (P-ABA) was bought from Merck KGaA. Monopotassium phosphate and dipotassium phosphate for phosphate buffer solution (PBS) were purchased from P.P.H. "STANLAB". Double-distilled water (dd H_2O) was used to prepare all aqueous solutions. Air Products delivered refrigerated argon. All reagents were used without prior purification and stored according to the manufacturers' instructions.

Biological materials utilised in this work, i.e., monoclonal mouse IgG2B anti-SARS-CoV-2 Spike RBD antibodies (MAB1054), recombinant SARS-CoV-2 Spike RBD (HEK: 10500-CV, CHO: 10534-CV), recombinant Human ACE2 (933-ZN), and recombinant Human CD147 Fc Chimera (972-EMN) were obtained from R&D Systems. IgG2B and CD147 were labelled with a C-terminal 6-His tag, and ACE2 was labelled with a C-terminal 10-His tag. All materials were used without prior purification and were prepared and stored according to the manufacturers' instructions.

2.2. Boron-doped diamond electrode fabrication procedure

The BDD electrodes were prepared using a microwave plasma-enhanced chemical vapour deposition (MWPECVD) system (SEKI Technotron AX5400S, Japan). BDD electrodes were grown on p-type (100)-oriented silicon substrates. The nucleation of the substrates was carried out via sonication in a nanodiamond suspension (crystallite size of 5–10 nm) for 1 h [28]. During deposition, the process temperature of the substrate was kept at 700 °C. Microwave radiation (2.45 GHz) was used to excite plasma ignition. The plasma microwave power, optimised for diamond synthesis, was kept at 1300 W. The gas mixture ratio was 1% of the molar ratio of CH_4–H_2 at the gas volume of 300 sccm of the total flow rate. The process pressure was kept at 50 Torr, and the base

pressure was approximately 10^{-6} Torr. All samples were doped using a diborane (B_2H_6) dopant precursor; [B]/[C] ratio was 10,000 ppm in the plasma. Synthesis was carried out for 12 h resulting in a film thickness of ca. 6 μm [29,30].

2.3. Biofunctionalisation procedure of boron-doped diamond electrode

The BDD electrodes used in these studies were biofunctionalised to enhance the antibody-antigen interaction of the sensor. Before biofunctionalisation, the BDD electrodes were washed in an ultrasonic cleaner with methanol and dd H_2O for 5 min each. The electrochemical properties of each electrode were then evaluated. All electrodes studied had an anodic-to-cathodic peak ratio close to one (for $[Fe(CN)_6]^{4-/3-}$), with peak separation $\Delta E < 100$ mV. The charge transfer resistance of the unmodified electrode did not exceed 150 Ω in the studied electrolyte. These results indicate a reversible, diffusion-controlled electrochemical process at the unmodified BDD electrode surface. Consecutive measurements were carried out at each subsequent modification stage to determine the changes taking place on the surface of the sample.

In the first biofunctionalisation step 1 (FS-1), the electrode was modified with diazonium salt molecules, whose synthesis is presented elsewhere [31]. The obtained reagent was stored in the dark at − 20 °C. For electrode modification, a 50 mM solution of $Et_4N(BF_4)$ in acetonitrile was prepared, deoxygenated, and cooled. The synthesised diazonium salt was then added to obtain a solution with a concentration of 2.5 mM. This solution was used directly for electrografting, which was performed by polarising the working electrode (0.39 cm^2) from 0.1 V to − 1.0 V vs. Ag=AgCl|3 M KCl for six cycles using a scan rate of 100 mV/s. A current reduction peak at approximately 0.2 V indicated that the process was successful (Supplementary Information **file, section S1**). [32–34] Additional confirmation is given by the subsequent CV studies, where the ΔE increased to 380 mV and significant peak asymmetry was found due to the formation of a sealed monolayer hindering the charge transfer at the electrode interface [35,36]. Next, the sample was washed with methanol and dd H_2O and dried with an argon stream.

Biofunctionalisation step 2 (FS-2) consisted of incubating the sample in 100 mM EDC solution (pH = 5.7) and 50 mM NHS (pH = 8) in PBS both for 30 min at room temperature, and functionalisation step 3 (FS-3) in 60 mM NTA solution in a bicarbonate buffer (pH = 10.4) for 2 h at room temperature. Next, the electrode was incubated for one hour in an aqueous $NiCl_2$ solution at the same temperature as in the previous stages, which constituted the next functionalisation step (FS-4). In the next step (FS-5), the electrode was incubated in a solution of one of the three receptors in PBS (pH = 7.4) for 16 h at 5 °C. The receptors used are summarised with the parameters in Table 1 together with the acronyms that are further used in the text. The concentration of each receptor was always 3.33 μg/mL. In the last functionalisation step (FS-6), the electrode was incubated in 0.05% BSA in PBS (pH 7.4) for 15 min at 5 °C to saturate the free spaces on the surface of the electrode and prevent the non-specific binding of the protein [37]. After each step, the electrode was rinsed with dd H_2O and dried with argon. The volume of solution used for the modification was always 75 μL. After modification of the electrodes, the system's response to the blank test was checked. For this purpose, 75 μL of PBS solution (pH = 7.4) was applied, and the EIS measurement was performed. When the value of R_{CT} was close to the value of the previous step, the system was considered stable. The functionalisation steps are schematically shown in Fig. 2, and the simplified schema of functionalisation with one extra step is shown in the Supplementary Information **file, section S2**.

The PBS solution (pH = 7.4) containing the tested analyte and the SARS-CoV-2 spike S1 protein RBD (SARS-CoV-2 RBD) with a concentration range of 0.30–64 ng/mL, was put on the electrode. The drop-casted volume was 75 μL and the solution was left for 15 min incubation at a temperature of 5 °C. The electrodes were washed with demineralised water, gently dried with a stream of argon, and taken for electrochemical measurements.

2.4. Dynamic electrochemical impedance spectroscopy procedures

All electrochemical measurements were carried out in a three-electrode system using a potentiostat SP-300 (Biologic). Classic electrochemical impedance spectroscopy (EIS) and cyclic voltammetry (CV) were performed next to the DEIS measurements. The electrolyte was 1 mM $K_3[Fe(CN)_6]$ and 1 mM $K_4[Fe(CN)_6]$ in PBS (pH 7.4), deoxidised by passing through a stream of argon prior to measurement. The electrolyte volume was 1 mL. A platinum wire was used as the counter electrode. The reference electrode was an Ag=AgCl|3 M KCl for CV and EIS measurements and a silver wire coated with silver chloride for the DEIS studies. The working electrode was the functionalised BDD with an electrolyte-exposed surface area of 0.196 cm^2. During the DEIS measurements, the reference was a silver wire coated with silver chloride.

The Dynamic Electrochemical Impedance Spectroscopy measurements were conducted in potentiodynamic polarisation mode (pDEIS), where the multisine AC perturbation is superimposed with the linearly-variable DC polarisation (CV scan). The AC perturbation signal was composed of 30 elementary sine waves in the frequency range of 24.5 kHz to 3 Hz. The phase shifts of each elementary signal were selected using optimisation software written in the LabView environment to minimise the resultant multisine signal peak-to-peak amplitude, which did not exceed 15 mV in this case. Details on the construction of the multisine perturbation signal are presented elsewhere [38]. The response signal was sequenced into portions (one second in length) and Fourier-transformed. When choosing a scan rate, the limiting factor is the length of the single portion of the signal used for the Fourier Transformation. The polarisation scan rate was set at 5 mV/s. The length of a single portion was selected as 1 s, keeping in mind the lowest frequency of the elementary signal used. These conditions made it possible to obtain *quasi*-stationary conditions throughout the measurement duration, without spectra leakage. Three consecutive DC polarisation scans were carried out starting from the formal redox pair potential ($E^{0'} \approx 0.12$ V), in the polarisation range between − 0.50 and + 0.75 V vs. Ag=AgCl. The exemplary resultant 3D pDEIS spectrum in the Nyquist plot, with applied polarisation potential at the Z-axis, is presented in Fig. 1A. Impedance spectra were collected every 10 s. The corresponding, simultaneously registered CV scan is given in Fig. 1B. Fig. 1C–F depict pDEIS impedance spectra, each obtained under notable polarisation conditions, i.e. near the cathodic and anodic polarisation limits (Fig. 1C and D, respectively), $Fe(CN)_6^{4-}$ oxidation peak (Fig. 1E), $Fe(CN)_6^{3-}$ reduction peak (Fig. 1F).

The resultant instantaneous impedance spectra were subjected to the

Table 1
SARS-CoV-2 receptors used for biofunctionalisation of the BDD electrodes in FS-5. Dimensions and atom counts of receptors are calculated from their crystal structures (IgG2B, ACE2) or models (CD147). Isoelectric points and total charge (in |e|) are calculated from their sequences using Protein Calculator v3.4 (protcalc.net).

Receptor	Acronym	Atom count	Dimensions	Isoelectric point (pI)	Charge (at pH=7)
IgG2B anti-SARS-CoV-2 Spike RBD antibodies (MAB1054)	IgG2B	~20,000	16 × 11 nm (144.9 kDa)	7.42	+ 5.8
angiotensin-converting enzyme ACE2 (933-ZN) dimer	ACE2	~ 23,400	16 × 2 nm (170 kDa)	5.94	-33.8
CD147 Fc Chimera (972-EMN)	CD147	~ 6600	15 × 6 nm (47.5 kDa)	6.53	-5.0

Protein Calculator v3.4: protcalc.sourceforge.net
Source:Sourceforge.

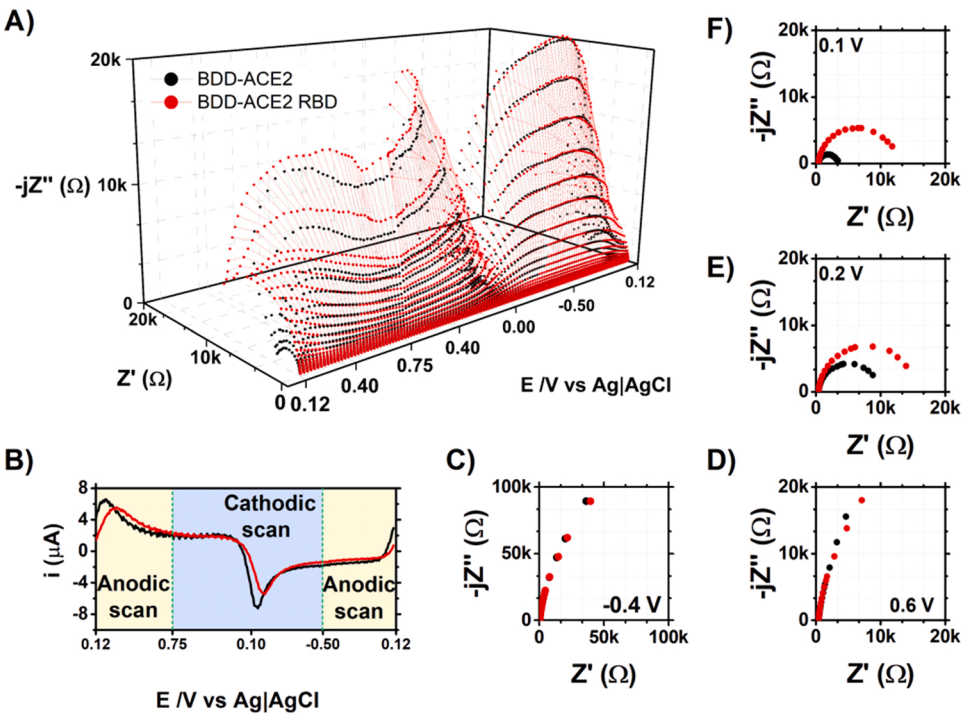

Fig. 1. pDEIS data recorded for ACE2 receptor grafted onto BDD with and without the presence of SARS-CoV-2 RBD. A) 3D impedance spectra with the applied polarisation potential on the Z-axis, and B) corresponding cyclic voltammogram registered during the pDEIS measurement. pDEIS impedance spectra clippings in the classic Nyquist projection obtained during polarisation at characteristic polarisation potential values: C) − 0.4 V, D) + 0.6 V, E) + 0.2 V (anodic scan) and F) + 0.1 V (cathodic scan). Scan rate 5 mV/s.

fitting procedure using an equivalent electric circuit (EEC). Dedicated software in the LabView environment was written for this purpose due to the many individual spectra to be analysed. The EEC used for the analysis was a modified Randles circuit, characterised by series resistance (R_S) and parallel connection of charge transfer resistance (R_{CT}) and constant phase element (CPE), used instead of a capacitor to describe the *quasi*-capacitive character of the electric double layer and receptor-functionalised film at the heterogeneous electrode surface [39]. The impedance of CPE is defined as (1):

$$Z_{CPE} = \frac{1}{Q(j\omega)^{\alpha}} \tag{1}$$

where Q is the *quasi*-capacitance, α is the so-called homogeneity factor (α = 1 for an ideal capacitor), ω is the angular frequency, and *j* is the imaginary number. The *quasi*-capacitance Q unit ($Fs^{1-\alpha}$) has no physical meaning; however, effective capacitance, C_{eff}, in F may be estimated with surface or normal time-constant dispersion models. We have calculated C_{eff} using the surface distribution function proposed by Hirschorn et al. [39] (2):

$$C_{eff} = Q^{\frac{1}{\alpha}}\left(\frac{R_S R_{CT}}{R_S + R_{CT}}\right)^{\left(\frac{1-\alpha}{\alpha}\right)} \tag{2}$$

The Warburg element was not included due to the frequency range used in the pDEIS experiment, with 3 Hz as the lowest elementary frequency used in the multisine perturbation signal. The EEC used in the pDEIS examination was labelled R(QR). More information about the specific pDEIS conditions and the EEC used for the purpose of electrochemical biosensing by our group can be found elsewhere [27].

For reference purposes, classic CV measurements were performed from − 0.5 to + 0.75 V vs. Ag=AgCl|3MKCl with a polarisation rate of 50 mV/s over three cycles. After determining the formal redox pair potential ($E^{0'}$) from the voltammogram, the EIS measurement was performed for the sample polarised for 30 s to the potential $E^{0'}$ before the measurement. The measurement was performed in the frequency range from 10 kHz to 0.1 Hz at 11 points per decade. The amplitude of the excitation signal was 10 mV. The EEC used for the EIS studies was similar to pDEIS, with the Warburg element added in series with R_{CT}. This EEC was labelled R(Q(RW)) and is often found in electrochemical biosensor studies [40,41].

2.5. Physicochemical studies

After each functionalisation step, the high-resolution X-ray Photoelectron Spectroscopy (XPS) spectra were recorded to verify their efficiency. These studies were carried out in the core level binding energy of C 1 s, N 1 s, O 1 s and Ni 2p photoelectron peaks, using an Escalab 250Xi multispectroscope (ThermoFisher Scientific). An X-Ray AlKα spot diameter of 650 μm was used, with a pass energy of 20 eV. The electric charge was controlled through a low-energy electron and low-energy Ar+ ion flow, with final peak calibration using adventitious carbon C 1 s at 284.6 eV. The deconvolution procedure was performed with the Advantage v5.9925 software (ThermoFisher Scientific).

2.6. Statistical and multivariate data analysis

The complete data matrix, including the EEC fit results of the DEIS measurements at different polarisation potentials, contained 2628 variables (R_S, Q, α, R_{CT}, C_{eff}, t, E, I for each of the 375 potential steps and the information about the receptor type, functionalisation step, and protein concentration) for 37 observations (experiments). Here, t, E, and I represent the instantaneous values of time, polarisation potential, and current recorded during the DEIS measurement, respectively. Data manipulation and elaboration were performed in R [42]. Principal Component Analysis (PCA) and Partial Least Square (PLS) regression were performed after mean-centreing, scaling, and removing the outliers from the dataset using the FactoMineR [43] and mdatools [44] packages. A restricted dataset consisting of 95 variables was obtained by dropping the highly correlated variables (corr>0.95), using the FindCorr function [45]. A schematic description is reported in the Supplementary Information **file, section S6**.

2.7. Molecular modelling of biosensing interface

The model of the recombinant Human ACE2 was prepared based on

the crystal structure of this protein (PDB code: 6M17) [46]. The crystal structure of ACE2 was modified by: (a) manually adding residues 18–20, (b) removing residues 750–805, and (c) replacing residues 740–750 with a 10-His-tag by preserving the backbone of the protein and *in-silico* mutation of the IWLIVFGVVM fragment to HHHHHHHHHH. [46]. This ACE2 model was placed on a model of a BDD electrode consisting of 100 (10 × 10) NTA molecules, terminated with a methyl group and aligned in the xy plane with the spacing corresponding to the optimal spacing of the NTA molecules on the BDD electrode. NTA molecule models were created based on the DFT-optimised NTA geometries used earlier [47], but did not contain Ni^{2+} ions and had all carboxyl groups protonated, so their formal total charge was equal to zero. ACE2 was placed on the BDD electrode model in such a manner that two terminal His residues (749 and 750) were close to one NTA molecule and the positions of the NE2 atoms of each of those HIS residues were restrained using a 10,000 kcal/mol force constant in each dimension, together with the positions of the two terminal carbon atoms of each NTA molecule.

The model of the CD147 receptor, consisting of basigin and IgG1 fragments connected with a linker and terminated with a 6-His tag was prepared using the RoseTTAFold method implemented in the Robetta software [48]. This model was placed on the same BDD electrode as above in such a manner that two terminal His residues (424 and 425) were close to one NTA molecule and the positions of the NE2 atoms of each of those HIS residues were restrained using a 10,000 kcal/mol force constant in each dimension, together with the positions of the two terminal carbon atoms of each NTA molecule.

These two model systems were subject to 10 ns NVT equilibration followed by 500 ns of NPT MD runs using the CHARMM36 force-field [49] and the GROMACS 2020 software [50]. Fig. 6 was prepared using QuteMol ver 0.4.1 and PyMOL (The PyMOL Molecular Graphics System, Version 2.0 Schrödinger, LLC.) [51]. Protein-protein docking to model the interface between the CD147 and spike RBD protein was performed using the HADDOCK2.4 web server [52] and the obtained results were similar to the results obtained earlier [53].

3. Results and discussion

3.1. Effect of BDD electrode biofunctionalisation and its response to SARS-CoV-2 RBD

The biofunctionalisation procedure is presented in detail in Section 2.2, while its schematic representation is shown in Fig. 2A. The efficiency of each functionalisation step was confirmed using high-resolution XPS analysis. The key O 1 s and Ni 2p spectra are presented as a part of Fig. 2A, while all of the registered XPS results are presented and discussed in detail in the Supplementary Information file, section S3.

An increase in the amount of C═O bonds was found due to benzoic acid electrografting (FS-1), tracked with O 1 s signals at approximately 532.2 and 531.1 eV, corresponding to carbonyls and hydroxyls, respectively [54,55]. A simultaneous increase in the C 1 s C═O peak intensity can be tracked in the Supplementary Information file, Fig. S3 and Table S1. Next, successful incubation in an aqueous $NiCl_2$ solution (FS-4) was confirmed by the formation of a nickel ligand complex, represented by a Ni $2p_{3/2}$ signal at 856.0 eV, in the typical binding energy range of Ni-OH bonds [56]. A strong Ni $2p_{3/2}$ $Ni(OH)_2$ satellite feature was also recognised at approx. 862 eV. The macromolecular compounds introduced during the anchoring of the receptor protein (ACE2 as an example) within FS-5 were too complex for a detailed XPS analysis. However, a few characteristic features can be distinguished, including a significant increase (by 50%) in the N 1 s signal attributed to C-N bonds from proteinogenic amino acids [27,57]. The XPS results allowed us to observe an increase in the functionalisation layer thickness based on the intensity of the C 1 s spectra.

Furthermore, EIS and CV studies were carried out after each functionalisation step. A detailed analysis of these results is presented in the

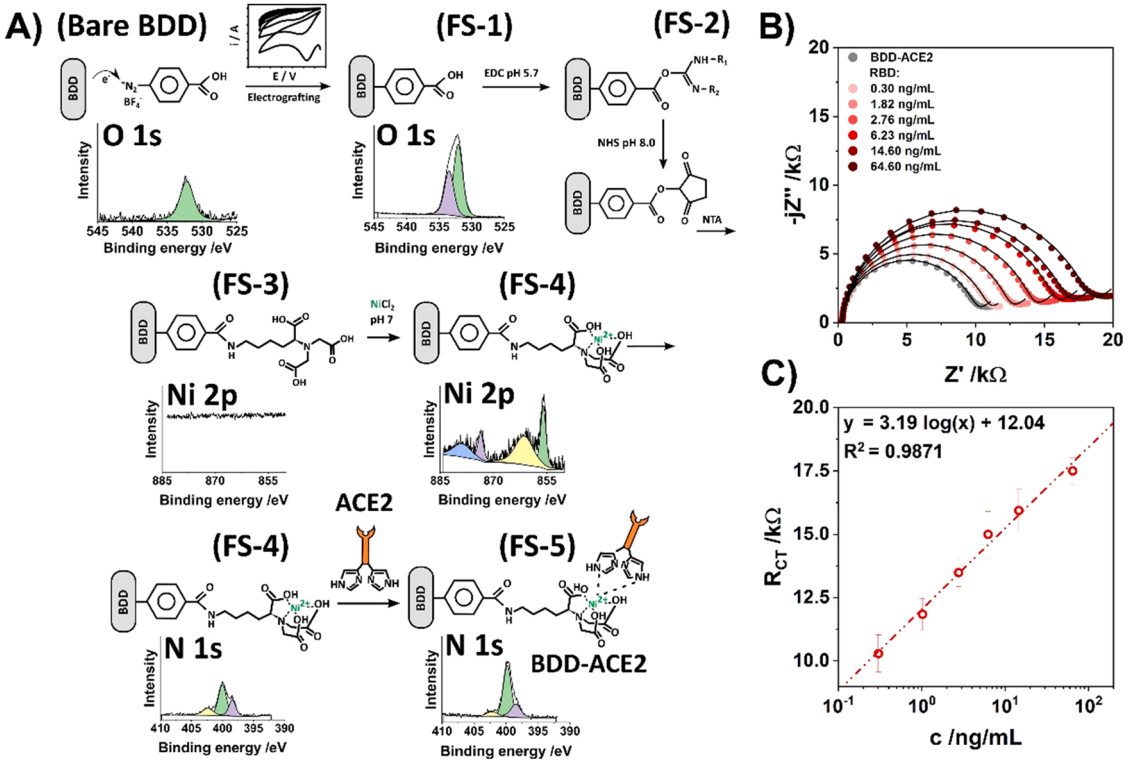

Fig. 2. A) Schematic BDD electrode functionalisation steps for ACE2 receptor, and key high-resolution XPS spectra recorded in the O 1 s and Ni 2p binding energy range, verifying successful electrode surface functionalisation; B,C) BDD-ACE2 biosensor verification: B) EIS spectra in the Nyquist projection and C) R_{CT} vs. SARS-CoV-2 RBD concentration function. Measurements at formal potential E = 0.12 V.

Supplementary Information file, section S4, allowing us to draw the following conclusions. The discussed changes in electric parameters hint at the formation of a benzoic acid layer, which reduces the electrochemically active surface area (EASA) after FS-1. On the other hand, activation of carboxyl groups with EDC and NHS (FS-2), and further NTA anchoring (FS-3) prove, in turn, the increase in electron transfer kinetics. Such phenomena were confirmed previously in the literature [58–60], suggesting that the functional groups formed at the electrode surface promote efficient charge transfer. Finally, anchoring the electrically-inactive receptor (FS-5) and BSA (FS-6) significantly hinders the charge transfer process. Thus, both the XPS and electrochemical analyses corroborate each other, affirming the efficacy of the applied functionalisation steps. Additionally, thanks to the monitoring of the electrochemical parameters of each sample before the functionalisation process and subsequently at each functionalisation step for multiple samples, the reproducibility of the functionalisation process has been confirmed and enhanced by eliminating samples with inappropriate parameters.

The detection capability of the sensors was first verified by tracking R_{CT} changes in a classic EIS study for different concentrations of SARS-CoV-2 RBD. The objective of this study was to evaluate the quantitative analysis capabilities and to evaluate the limits of detection (LOD) where the RBD binding is changing the electrode response for $Fe(CN)_6^{4-/3-}$, which is dissolved in solution. Fig. 2B presents the impedance spectra of BDD functionalised with the ACE2 receptor, incubated in a solution of PBS without RBD (blank) and with different concentrations of SARS-CoV-2 RBD. The EEC fittings are given in the Supplementary Information file, section S4, together with and the results for the two remaining receptors. The estimated R_{CT} values changing with the protein S concentration for the ACE2-functionalised electrode are presented in Fig. 2C. Each ACE2 peptidase domain can be treated as an active adsorption centre, accommodating one RBD molecule [46,61]. 20 residues of ACE2 and 17 residues from the RBD make direct networks of hydrophilic, side chain interactions with an interface area of 863 Å [4]. The R_{CT} increases as the RBD concentration increases, showing high correlation with the logarithmic function (as seen in Fig. 2C) in a wide concentration range, which is connected with RBD adsorption at the electrode surface. Proteins adsorption is commonly interpreted to follow the Langmuir mechanism of adsorption, however, the fundamental assumptions of this model are not met for very complex structures of proteins and multiple properties affecting the adsorption [62,63]. The logarithmic nature of the discussed relationship makes it impossible to determine the LOD using the standard formula which utilises the slope of the calibration curve presented in Fig. 2C and the standard deviation of the response:

$$LOD = 3.3 \bullet \left(\frac{S}{a}\right) \quad (3)$$

where S is the standard deviation of the response, and a is the slope of the linear calibration curve [64]. Instead, another approach was proposed here, based on the concentration of protein S corresponding to the exact same change of sample impedance as it would be for the blank or any other negative sample. Using the R_{CT} of the blank (PBS) sample, 9.46 kΩ, and the equation from Fig. 2C, the LOD value for ACE2 was estimated as 0.157 ng/mL. The LOD estimates for the remaining two receptors are: 0.025 ng/mL (IgG2B) and 0.096 ng/mL (CD147), see the Supplementary Information file, section S5 (Figs S5A-C) for details.

3.2. Molecular modelling

Finally, to obtain more atomic-level information, we performed

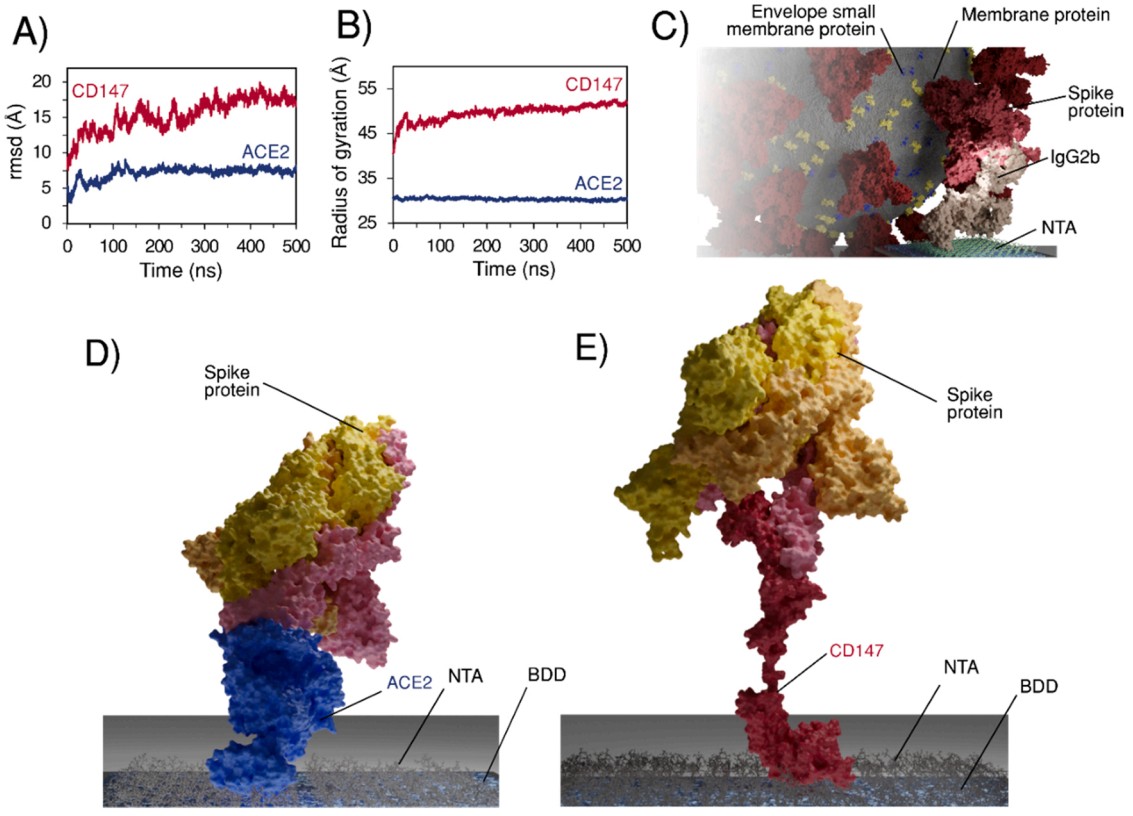

Fig. 3. Molecular dynamic of biofunctionalised BDD interface: A) rmsd and B) radius of gyration of ACE2 (red) and CD147 (blue) on the surface; C) Scheme of the interaction of SARS-CoV-2 envelope protein with assay; D) visualisation of the spike protein from the crystal structure of SARS-CoV-2 S superimposed on the final snapshot of ACE2 on the NTA-functionalised surface; E) visualisation of the spike protein from the crystal structure of the SARS-CoV-2 S-ACE2 complex [69] superimposed on the final snapshot of CD147 on the NTA-functionalised surface;.

molecular dynamics (MD) studies, (for other computational studies of electrochemical experiments on proteins see [65–68]). We prepared models of ACE2 and CD147 receptors on the functionalised sensor (see Methods) and performed 500 ns MD runs. Fig. 3 shows the starting and final conformations of the ACE2 protein on the sensor surface, together with the selected statistical data (root-mean-square deviation (rmsd) of the atomic positions with respect to the ACE2 crystal structure and radius of gyration) along the entire simulation. One can see that visually both receptors acquire different conformations and this is also reflected by the relatively high rmsd and radius of gyration values, suggesting that the conformational changes within both receptors immobilised on the surface are relatively large. A more detailed analysis of the ACE2 interface directly interacting with the spike RBD (residues 18–45 and 350–355) reveals that it remains virtually unchanged in the course of the simulation, with the rmsd of the 500 ns snapshot versus the crystal structure of 0.93 Å (all-atom) and 0.61 Å (backbone), see Fig. 6E. The same is true for CD147, as the CD147 interface is predicted to interact directly with the spike RBD (residues 1–21, 109–116 and 165–171) with a rmsd of the 500 ns snapshot versus the 0 ns snapshot of 5.30 Å (all-atom) and 4.33 Å (backbone). As a result, we can expect that in both cases the possibility of spike protein recognition remains very high, which is likely the result of the fact that the spike RBD binding regions are relatively far from the surface (around 8 nm from the surface for both studied receptors, based on the final snapshots of the molecular dynamics runs).

The density of the ACE2 coverage depends on the orientation of the protein on the surface. Our studies suggest that the optimal orientation is with the Spike protein-recognition region oriented away from the surface and able to bind Spike protein. We can, however, estimate the maximum theoretical coverage of ACE2 based on two extreme orientations, one with the receptors pointing away from the surface (as in Fig. 3) and one with the receptors lying flat on the surface. Based on estimate of surface coverage, one molecule of ACE2 in the minimum-surface coverage orientation takes up surface area of approximately 7500 $Å^2$, which results in a density of 13,000 ACE2 molecules/μm^2, while in the maximum-surface coverage orientation it is 12,500 $Å^2$ and 8000 ACE2 molecules/μm^2, respectively. For CD147, these values are 2100 $Å^2$ (~48,000 CD147 molecules/μm^2) for the minimum-surface coverage orientation and 9800 $Å^2$ (~10,000 CD147 molecules/μm^2) for the maximum-surface coverage orientation.

3.3. PCA and PLS regression of pDEIS impedimetric data

PCA can be used to help identify clusters in the data or find outliers. In particular, the latter one was used for data pre-treatment. When dealing with large datasets, such as in the current example, where a single experiment comprises thousands of derived variables, it is important to have a tool able to screen the correctness of the measured values quickly. The novelty is applying such a concept to two differently structured datasets to find different types of outliers. Firstly, since the dataset was generated by applying an automatic fitting algorithm on the raw impedance spectra, the aim was to check the correctness of the EEC fit results at a specifically applied bias. Secondly, the objective was to identify possible experiment outliers caused by the loss of control during the experiment. These two objectives were successfully pursued by applying PCA at differently merged datasets. Conducting PCA on the separated datasets (one for each experiment), where each row is constituted by the 375 applied bias and the column by the results of the EEC fitting, allowed us to find outliers caused by the algorithm. Instead, conducting PCA on the aggregated dataset, where each row is one experiment and the columns are the resulting EEC fitted parameters at the 375 measuring steps, it is possible to highlight the experiments which do not appear in clusters, thus, in which a loss of control during the experiment may have happened. Moreover, PCA was employed to explore the intrinsic patterns. To do so, the abovementioned data pre-treatment and outlier detection and elimination was a necessary step.

PCA was initially performed on the EEC fitting results at a different potential, on a single test, in order to identify the outliers relative to the single measurement of 13,875 observations, 5 were replaced with the column-averaged value (see the Supplementary Information file, section S6). Subsequently, the data was aggregated into 37 observations, each row consisting of a single test, and the 2628 columns were the fitted EEC components at different potentials. After performing scaling and centring of all of the variables, PCA was performed again on the cleaned dataset to highlight possible clusters and outliers. Two tests were identified and removed from the dataset. After a more in-depth analysis, one sample was characterised by an abnormal shift of the R_{CT} peak during the polarisation scan, originating from the irreversible character of the charge transfer process at the contaminated electrode surface. The other sample was lost by experimental control. Due to the small potential step applied between two subsequent pDEIS measurements, which may cause similar system responses, and to the three polarisation sweep repetition, multicollinearity was found among the variables. For this reason, variables having a mean absolute correlation greater than 0.95 (arbitrarily set as the threshold) have been removed from the dataset [45].

The details of the discussed PCA analysis are presented in the Supplementary Information file, section S6. PCA was conducted on the reduced dataset, and the first five principal components (PCs) explained 81.4% of the total variance; however, the first two components accounted for only 23.1% and 18.5%, respectively (Fig. S8A). For this reason, we decided to restrict the analysis to the description of the first five axes. The SARS-CoV-2 RBD concentration was supplied as a continuous supplementary variable, together with its log-transformation, and positioned in the factorial spaces using the same transformation applied to the active variables. As can be seen in Fig. S8B, among the first five dimensions, the most significant contribution is projected into PC2, PC3 and PC4. When considering the receptor type as a supplementary category, it is possible to see the highest opposition in PC3 between ACE2 and the group formed by IgG2B and CD147, and in PC4 between ACE2 and IgG2B. The projection of the tests into the space defined by PC2 and PC3 is reported in Fig. S8D, and the colour is representative of the SARS-CoV-2 RBD concentration.

The regression performed using the equivalent circuit parameters provided the best correlations compared to the one performed on the raw impedimetric data (Supplementary Information file, Fig. S6). Moreover, in both cases, the preliminary reduction of highly-correlated variables improved the quality of the features extraction. The optimal number of components for the PLS regression was estimated by permutation and was set to five (Fig. 4A). On the other hand, Fig. 4B shows the correlation between the experimental values and those obtained by the PLS prediction model using five latent variables. For ease of comparison, the Variable Importance in Projection (VIP) scores (Fig. 4D), which estimate the significance of each variable in the PLS projection, have been reported in addition to the typical averaged current–potential plot for a specific electrode (Fig. 4C). A threshold of 1.2 was chosen to further highlight the predictor variables that best explain the concentration variance (Fig. 4D, dotted line).

It is possible to observe that most of the variables characterised by a high VIP belong to the first cycle, at positive electrode polarisation potentials (Fig. 4D, red). However, the highest VIP value belongs to the average current, i, measured during electrode polarisation between − 0.20 and − 0.17 V in the second cycle, during anodic polarisation. The full list of points of interest (POI) identified by the PLS regression is reported in the Supplementary Information file, Table S3. To include the receptor type in the PLS analysis, a dummy response variable was used, equal to + 1 for objects belonging to a class and 0 for those that do not. The CD147 receptor has the highest VIP, suggesting that it is more sensitive to changes in protein concentration. However, it is interesting to note that the CD147 and IgG2B coordinates in the new PLS space have opposite signs. Furthermore, from the PLS regression results, using the raw dataset (Supplementary Information file, Fig. S9), the VIP scores

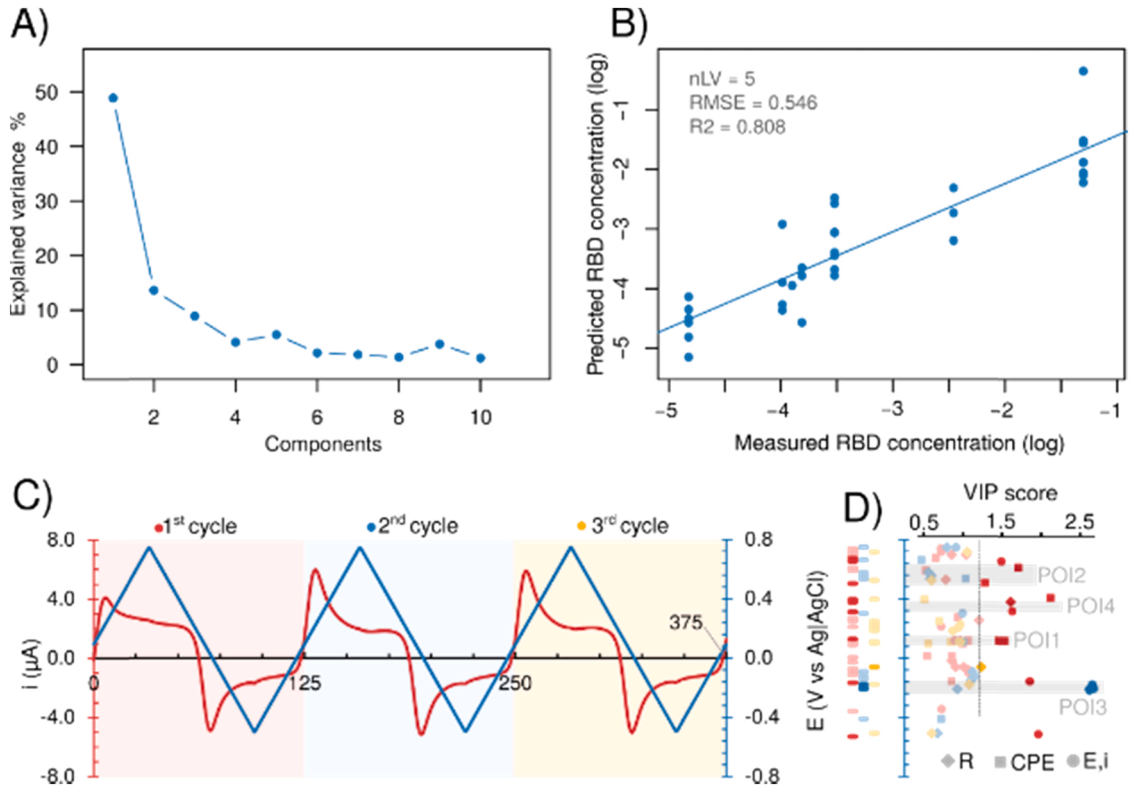

Fig. 4. PLS regression results and interpretation: A) explained variance as a function of the components; B) plot with predicted vs. measured (reference) concentration; C) example of i-E plot representative for one test; D) visualisation of the variable importance in projection as a function of E and the scan cycle.

suggest investigating the system at low (< 100 Hz) and high (≥ 19.1 kHz) frequencies. This feature will be studied in consecutive studies.

3.4. Detailed pDEIS analysis of the first full polarisation scan

The PCA and PLS examination for a wide variety of the electric parameters obtained from the pDEIS analysed using R(QR) EEC revealed characteristic changes with the applied DC polarisation. According to the variables kept after correlation and the VIP scores, the first polarisation cycle was found to provide the most meaningful and repetitive data, and thus we decided to focus on it in further analyses. In Fig. 5, we present the values of the pDEIS electric parameters, R_{CT}, C_{eff}, and α, with changes in the electrode polarisation. All the recorded changes origin

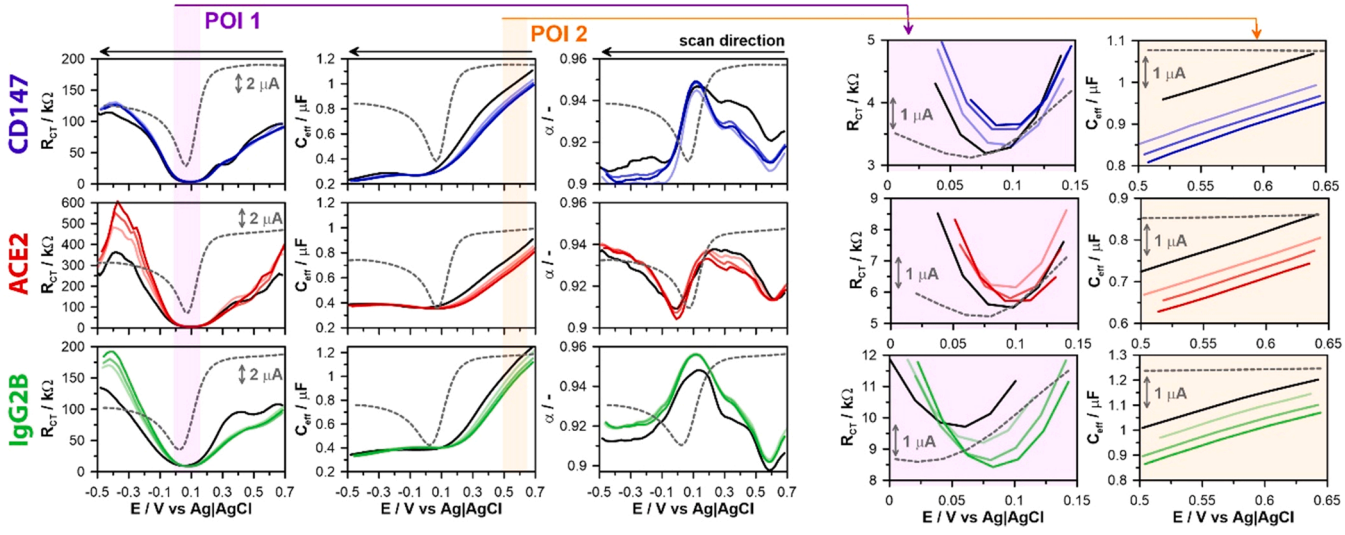

Fig. 5. To the left, the charge transfer resistance (R_{CT}), effective electric double-layer capacitance (C_{eff}), and CPE exponent (α) changes based on pDEIS results of the first cathodic polarisation scan. The BDD electrode was functionalised with one of the receptor proteins (CD147, ACE2, IgG2B). The test was performed in 1 mM $K_3[Fe(CN)_6]$ and 1 mM $K_4[Fe(CN)_6]$ in PBS solution (black line) as well as with SARS-CoV-2 RBD at different concentrations: 0.301, 3.47 and 50.0 ng/mL (coloured lines, darker with increasing concentration). The dashed line represents the corresponding cathodic currents. To the right, the magnified point of interest (POI) polarisation ranges, characterised with the highest differentiation of electric parameters R_{CT} and C_{eff} with SARS-CoV-2 RBD concentration, based on PCA and PLS analyses.

from alteration in the electrode response for $Fe(CN)_6^{4-/3-}$ resulting from receptor presence and RBD binding events. We have chosen to present the first scan in the cathodic direction as it is the first scan in the full polarisation range between + 0.75 and − 0.50 V vs. Ag=AgCl.

The results presented above shed light on the characteristic changes in electric parameters at the studied electrode surface that occur throughout the experiment. In general, the trend in changes of both R_{CT} and C_{eff} is similar regardless of the electrode-functionalised receptor protein, suggesting a similar SARS-CoV-2 RBD interaction mechanism. Small variations are only visible for the CPE exponent α between ACE2 and the remaining receptors (IgG2B and CD147), at a negatively charged electrode surface.

The minimum of the R_{CT}=f(E) function is strictly connected with the $[Fe(CN)_6]^{3-}$ reduction peak regardless of the studied system and the parameter only increases as a consequence of the relaxation process, when the charge accumulated at the electrode surface is consumed by the redox processes (Niedzialkowski et al., 2020). This effect surpasses the expected increase in polarisation resistance as a result of the lowering of the anodic overpotentials in the first phase (at positive potentials). The R_{CT} values measured for each receptor functionalisation may differ, which is a result of complex macromolecule interactions with the electrode (i.e. complementarity in surface charge distribution, geometry, hydrophobic interactions), functionalisation thickness and density, subtle electrode pre-treatment differences, etc. Importantly, the observed trends are independent of the initial electrode conditions. Despite the similarity in the trend of the R_{CT}=f(E) function, there are observable differences between the receptors when studying R_{CT} values at the negatively-charged electrode surface, with significantly higher resistance observed for ACE2 compared to IgG2B and CD147, further increasing with the anchored RBD concentration. The ACE2 dimer is negatively charged (−33.8) under the chosen experimental conditions (see Table 1), with strongly negatively charged sites, namely, a part of the metalloprotease's active site, or RBD docking region. Therefore, it can be expected that during its interaction with a negatively charged electrode surface, the electron transfer mechanism is hindered. Moreover, on reduction of the ferrocyanide ions, the negatively charged $[Fe(CN)_6]^{4-}$ migration may be affected by the repulsion force with the electrode surface. However, thanks to the electrostatic potential at the surface of the RBD's binding site, this receptor-target pair is highly complementary and is characterised with the strongest interaction among all studied receptors (Kd equal to 7.037×10^{-9} M) [70]. This topic is discussed further when introducing plausible interaction mechanisms (see Fig. 6G).

Nearing the potential of $[Fe(CN)_6]^{3-}$ to $[Fe(CN)_6]^{4-}$, the reduction effects in C_{eff} drop regardless of the type of receptor functionalisation, but the cause of this phenomenon is not fully understood. We speculate that it is due to the adsorption of the redox probe at the electrode surface and the restriction of the available EASA, according to Eq. (3) or/and the reduction of the oxidised $[Fe(CN)_6]^{3-}$ form available on the EASA. Further deep cathodic polarisation leads to an almost constant C_{eff} value. Only negligible differences in C_{eff} values are observed between the receptors, most noticeably at positively charged surfaces. The influence of the SARS-CoV-2 RBD concentration is visible at each polarisation step, where the increase in concentration causes the C_{eff} drop, as discussed later on.

Finally, the α value increases at the beginning of the scan in the cathodic direction, always peaking in the vicinity of the $[Fe(CN)_6]^{3-}$ ions reduction potential and decreasing afterwards. This drop is primarily related to the increase in electric heterogeneity due to the appearance of varying $[Fe(CN)_6]^{4-}$ and $[Fe(CN)_6]^{3-}$ concentrations in the diffusion layer. Here again, an important distinction between ACE2 and other receptors has been observed. In the case of ACE2, the electric

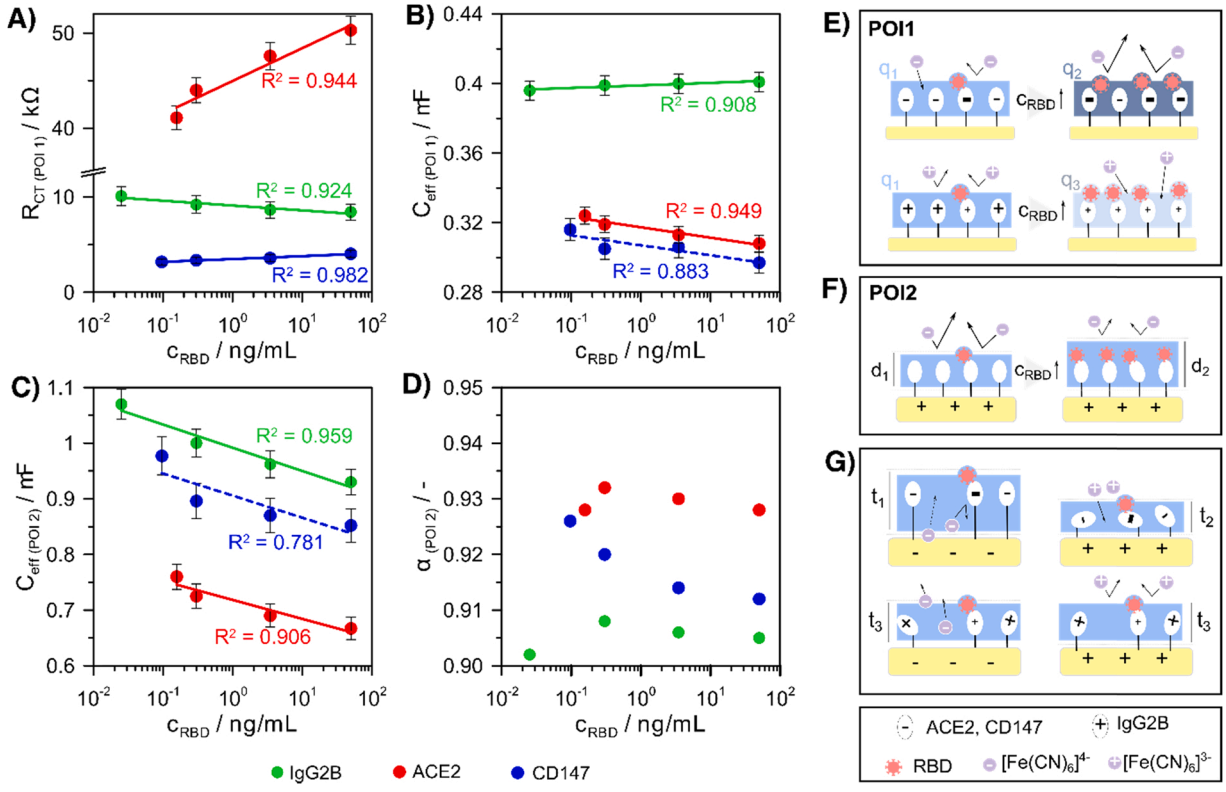

Fig. 6. A–D) pDEIS electric parameter changes with SARS-CoV-2 RBD concentration, values recorded for A) R_{CT} and B) C_{eff} at POI1; C) C_{eff} and D) α at POI2. Solid lines represents statistically significant relationship ($p < 0.05$). The POIs were determined based on PCA and PLS analyses. E–G) Schematic protein – protein interaction mechanism of the BDD surface functionalised by cellular receptor due to: E) changes in film charge (q_{1-3}) at POI1, on RBD anchoring; F) changes in film thickness (d_{1-2}) at POI2, on RBD anchoring; G) other plausible changes caused by electrostatic forces and affecting functionalised layer thickness (t_{1-3}) at the negatively- and positively-charged electrode surface.

homogeneity appears to secondarily increase at the negatively charged electrode's surface. We introduce a plausible explanation for this phenomenon later, when discussing Fig. 6G.

Based on the PCA and PLS examination, POI's were selected revealing the polarisation conditions at which the greatest influence of the SARS-CoV-2 RBD concentration on the studied electric parameters of the assay is anticipated. The instantaneous values of these parameters in the aforementioned POI's are plotted in Fig. 6A–D as a function of the RBD concentration. In Fig. 6, the reference zero RBD concentration studies were plotted at the respective LOD concentrations for each studied receptor (Supplementary Information file, Fig. S5).

POI1 corresponds to the electrode polarisation range of the $[Fe(CN)_6]^{3-}$ to $[Fe(CN)_6]^{4-}$ reduction potential. Here, intuitively, the charge transfer process is the most sensitive to the chemical state on the electrode surface and RBD anchoring, thus tracking the R_{CT} parameter is of particular value. It should also be noted that the $[Fe(CN)_6]^{3-}$ reduction peak potential depends on the reversibility of the redox process and thus may slightly differ between the studied receptors. Based on experimental findings, POI1 was set-up as 0.07 V vs Ag=AgCl for CD147 and ACE2 receptors and 0.04 V for IgG2B. The POI1 R_{CT} results reveal a very good correlation coefficient (R^2) with logarithmic function, as previously observed in the EIS studies (see Fig. 6A). It is generally expected that the R_{CT} will increase with the increase in the analyte concentration when anchoring at the electrode surface and, as a consequence, limit the available EASA. This relationship was found for both the ACE2 and CD147 receptors.

A surprising and difficult to explain reverse trend is observed for the IgG2B receptor. Its nature, however, was confirmed by the high R^2 value of the logarithmic function. The charge transfer kinetics depend to some extent on the electrostatic and non-electrostatic interactions between the electrode, the anchored layer and the redox probe, affecting the migration of the latter at the electrode vicinity [27,71]. Thus, a plausible explanation of the characteristic R_{CT} vs. RBD concentration for the IgG2B receptor may be hypothesised under the assumption of negatively-charged sites at the RBD. RBD anchoring to negatively-charged ACE2 and CD147 would maintain the negative charge of the functionalisation layer (Fig. 6**E**, top). Here, the resultant rise in R_{CT} is solely due to restriction in the availability of the EASA with the RBD concentration. However, in the case of a slightly positively-charged IgG2B receptor (Fig. 6E, bottom), RBD anchoring neutralises the overall charge of the functionalised layer. The higher the RBD concentration, the lower the repulsive electrostatic interaction with $[Fe(CN)_6]^{3-}$, thus the lower measured R_{CT}. Both of these effects are competitive. However, this hypothesis is based on the assumption that the RBD possesses negatively charged sites, while the RBD exhibits a formal charge of + 7. The formal charge depends on the local pH and pK_A, which could vary in the system and fluctuate with the applied AC potential. Additionally, these charges change when binding and interacting with each other (protein–surface, RBD–protein, etc.) and unfortunately there are no available computational methods to simulate a large and complex system on such a scale. A similar outcome was observed multiple times, in particular for nanoporous membrane-based sensors, and explained by the specific binding quenching the surface charge in the functionalized layer increasing the transient ionic conductivity [71,72]. The functionalized layer acts as a polyelectrolyte and may be characterized with nanopores based on the receptor grafting density. Gosai et al. [73] hypothesizes that binding thrombin to functionalized receptor locally increases counterion concentration required to balance the charges on the grafted biomolecules, resulting in an impedance decrease with analyte concentration.

According to the PLS results, the *quasi*-capacitance represented by C_{eff} offers the best defined character of changes with the SARS-CoV-2 RBD concentration at POI1. This parameter is presented in Fig. 6B. Indeed, the C_{eff} trends are expectedly opposite to those observed for R_{CT}. The dependence of C_{eff} on the RBD concentration reveals an inversely proportional logarithmic trend for the ACE2 and CD147 receptors. This effect was not observed for the IgG2B receptor, likewise for changes in R_{CT}. Since C_{eff} depends on R_{CT} by Eq. (2), it is possible that the ambiguous charge transfer mechanism affects both parameters.

Nevertheless, the most prominent changes in *quasi*-capacitance take place at high anodic potentials. The defined POI2 is the most suitable for characterisation of the analyte at the sensor surface (see Fig. 6C), and unlike at POI1, the C_{eff} drop with the RBD concentration increase is prominent regardless of the studied receptor. The character of the changes derives from the gradual increase in the functionalisation layer thickness on RBD anchoring at the electrode surface and consecutive EASA restriction, as visualised in Fig. 6F. Notably, the lowest C_{eff} values in Fig. 6C are seen for the ACE2 receptor, which is spatially the largest among all of the studied receptors. A similar observation was made by [74] while [75] suggest capacitance reduction due to displacement of counterions on RBD binding on the receptor. Notably, the surprising behaviour found for the IgG2B receptor in POI1 is no longer observed.

Finally, the characteristics of the CPE-related homogeneity factor α also graphed in POI2 (Fig. 6D) is too complex to show any reasonable trend of changes with the concentration of SARS-CoV-2 RBD. Generally, the results confirm the most electrically homogeneous film is formed by the ACE2 receptor, while the IgG2B receptor anchoring results in the most heterogeneous film. Being a significantly smaller molecule than any studied receptor, it appears that the RBD anchoring has only a negligible influence on the α value, but an increase in the RBD concentration still gradually decreases the observable differences between each studied system. Here, at the positively charged electrode surface, the deciding factors are believed to be the receptor-target binding constant and the interaction type, where the noncovalent interactions of the IgG2B receptor may lead to noticeable differences in the steric hindrance of the macromolecular system studied.

The observed DEIS effects revealed the complexity of the studied biosystems where the electrostatic and charging processes play an important role in the protein-protein interactions [27,76]. Other plausible charge effects affecting the migration of the redox ions by altering the functionalisation layer geometry at the polarised electrode surface are visualised in Fig. 6G. One should take into consideration that the electrostatic electrode surface–receptor repulsion/attraction forces (with or without anchored RBD) may alter both the functionalisation layer thickness and non-specific interactions of proteins in the electric field and steric hindrance effects. Ignoring factors other than the charge of the biomolecules, at cathodic polarisation the functionalisation layer thickness t_1 is expected to surpass t_3. The largely negatively-charged ACE2 receptor will be characterised by stronger repulsive forces against the BDD electrode surface compared to the more inert CD147 and IgG2B. The resultant modification of the functionalisation layer geometry may affect redox probe diffusion and migration pathways. These effects will also be significantly less prominent on anodic polarisation of the electrode.

The electrostatic potential at the surfaces of the relevant docking regions of ACE2 and RBD is highly complementary [70]. Therefore, ACE2 is characterised with the strongest interaction with SARS-CoV-2 RBD among the studied receptors, with the binding constant (Kd) equal to 7.037×10^{-9} M [70]. The pI of IgG2B equals 7.42, while its charge is slightly positive (+5.8) in the measurement conditions. IgG2B has a relatively homogeneous distribution of charges on the surface; therefore, it is difficult to distinguish negatively or positively charged sites. ACE2 is a transmembrane protein; however, the form immobilised at the electrode's surface is only the extracellular (EC) part of the protein (Gln18-Ser740). Therefore, the transmembrane (TM) part, which is the most hydrophobic part, is missing. Such changes do not influence the binding of the target (RBD), but likely have an impact on the behaviour of the protein at the sensor's surface. The C-terminus of ACE2 located closest to the electrode's surface (see the results of the molecular dynamics simulations presented below) consists mostly of neutral, nonpolar amino acids (e.g., VPPQNPPGLT – 739–730 aa). Therefore, except for the steric hindrance of the sensor's surface, this effect can be

intensified through amino acid groups that make the electrode-protein charge transfer more difficult. Additionally, the active site of ACE2 binds Zn^{2+} ions, which may further modify the electronic properties of the protein.

The control over the position and orientation of IgG2B during the covalent binding at the sensor's surface is a challenge. Most widely used conjugation/labelling methods do not provide sufficient control over the label's exact position, therefore, the optimal orientation of the IgG2B cannot be guaranteed [77]. This, in turn, can pose problems with a significant decrease in the antigen-binding activity. Each antibody may bind two RBD molecules through its Fab regions. Antibodies can approach and bind the RBDs at different angles. Usually, the RBD is bound to IgG2B through weak and noncovalent interactions such as electrostatic ones, hydrogen bonds, van der Waals forces, or hydrophobic interactions. The binding sites may overlap to different extents with the ACE2 binding site but the exact mechanism of the IgG2B-RBD interactions is still under debate. Depending on the binding site, the interface may vary from 626 $Å^2$ to 1248 $Å^2$ and may include from 9 to 35 contacted residues, therefore the exact K_d of its binding with the RBD is not known [78].

The CD147, in turn, is negatively charged under the studied conditions, with a pI of 5.94, yet significantly weaker than ACE2 and is presumably neutralised on RBD anchoring. The heptapeptide and IgG1 linked to CD147, closest to the sensor's surface, will determine the behaviour of CD147 during the electrochemical measurements. IgG1, like IgG2B, has a relatively homogeneous distribution of charges on the surface [79], possibly limiting the discussed effects. One should also take into consideration the significantly different $K_d = 1.85 \times 10^{-7}$ M [10] of the RBD binding and the fact that this is the smallest (47.5 kDa) of the studied compounds with possibly the smallest effects on steric hindrance.

In molecular dynamics, the charges are fixed and do not change during simulation, because the method does not allow it. Due to the size of the overall system, no other alternative method can be used. It should be noticed that additional effects may be effective in the real system, i.e. the whole biosystem can transform itself, as in Fig. 6**G**, after the DC signal is applied, which is not taken into account by the MD. The performed molecular dynamics does not show this, but the MD does not take into account AC signal transfer and the surface coverage with different proteins may be different. The antibody is much larger in size than ACE2 and CD147 and has a greater ability to "lie" partially on the surface. In addition, counterions existing in the biosystem can also determine charge transfer in the system.

4. Conclusions

In this study, an advanced multisine impedimetric analysis allowed us to reveal interactions in the SARS-CoV-2 spike RBD protein assay targeted by cellular receptors ACE2, CD147 and IgG2B. We also elaborated on the origin mechanism inducing variations of electrical parameters attributed to the molecular interactions driving RBD binding and recognition in presence of the redox probe dissolved in the electrolyte. Importantly, the impedimetric response, as described by the resistance of electric charge transfer through the electrode/electrolyte interface (R_{CT}) and receptor-functionalised film *quasi*-capacitance (C_{eff}) differed for the studied receptors as a result of the different complementarity of the surface charge distribution for the molecules, their geometry, hydrophobicity, and the thickness and density of the functionalisation biosystem. The designed assay with ACE2 provides a LOD value of 0.157 ng/mL. The LODs estimated for the other two receptors reached 0.096 ng/mL (CD147) and 0.025 ng/mL (IgG2B). This result is highly competitive to previous published findings, both in terms of LOD and test duration (see Supplementary Information file, Table S4 for more details).

The application of PCA to the experimental dataset allowed us to easily identify outliers and discriminate between the different receptors, while, the conducted PLS analysis, highlighted several POIs, which maximized the covariance between the logarithmic RBD concentration and the fitted EEC parameters, on which to conduct further analysis. These were in the vicinity of the redox reduction peak (POI1) and at anodic polarisation exceeding + 0.5 V vs. Ag=AgCl (POI2). At POI1, a different nature of R_{CT} changes was observed as a function of the RBD concentration for IgG2B. For ACE2 and CD147, R_{CT} increases with the concentration, which was attributed to the blocking of the electrochemically active electrode surface. There may be paths of conduction through the IgG2B in this state. The observation was followed by the inversely proportional *quasi*-capacitance changes, as expected. For the negatively charged electrode surface, R_{CT} was significantly higher for ACE2 than for IgG2B or CD147.

Significant differences in the electric *quasi*-capacitance of the functionalisation layers were recorded at POI2, especially for the positively charged electrode surface, while the trend of changes versus the polarisation function was analogous for each receptor. The lowest *quasi*-capacitances were noticed for ACE2, which we associate with the fact that this molecule is geometrically the largest, thus producing the thickest biosystem on the electrode surface. The discrepancies in the electrical homogeneity on the electrode surface, measured by the size of the frequency dispersion of the capacitance, were determined. Importantly, for ACE2 we observed the lowest capacitance values, regardless of its concentration, which can be explained by the size and charge of this macromolecule. Interestingly, changes in electrical homogeneity as a function of the RBD concentration do not provide unambiguous information, but the data confirm that the ACE2 receptor delivers the most homogeneous surface. This observation is especially correct for low RBD concentrations, while for higher RBD concentrations the differences in electrical homogeneity between electrodes with different receptors vanish.

The conducted DEIS study revealed a new insight into electrical effects which are consistent with previous observations [70] manifesting strong docking behaviour of ACE2 and RBD driven by the electrostatic potential. On the other hand, CD147 manifests significantly weaker interactions than ACE2 and is presumably neutralised on RBD anchoring. The presented approach allows for extended and ultra-sensitive studies such as rapid screening of physiological factors influencing cellular interactions, testing various mutations of SARS-CoV-2, and assessment of therapeutic drugs supporting and accelerating further in vitro, in vivo, and clinical investigations.

CRediT authorship contribution statement

Mateusz Brodowski: Validation, Investigation, Data curation, Writing – original draft, Visualization. **Mattia Pierpaoli**: Methodology, Validation, Formal analysis, Writing – original draft, Visualization. **Monika Janik**: Methodology, Writing – original draft. **Marcin Kowalski**: Investigation. **Mateusz Ficek**: Resources. **Pawel Slepski**: Software, Writing – review & editing. **Bartosz Trzaskowski**: Formal analysis, Writing – original draft, Visualization. **Greg Swain**: Writing – review & editing. **Jacek Ryl**: Conceptualization, Methodology, Investigation, Writing – original draft, Writing – review & editing, Visualization, Supervision, Funding acquisition. **Robert Bogdanowicz**: Conceptualization, Resources, Writing – review & editing, Supervision, Funding acquisition.

Declaration of Competing Interest

The authors declare that they have no known competing financial interests or personal relationships that could have appeared to influence the work reported in this paper.

Acknowledgements

This work was supported by the National Science Centre (Republic of

Poland) under projects “Express Call – Research on COVID-19” No. 2020/01/0/ST7/00104 (R.B.) and OPUS No. 2020/37/B/ST7/03262 (J. R.). M.J. acknowledge the support from the Foundation for Polish Science within START 2021 programme. Molecular modelling was performed on the Okeanos HPC at the Interdisciplinary Centre for Mathematical and Computational Modelling within the g86–1058 and g87–1079 grants.

Appendix A. Supporting information

Supplementary data associated with this article can be found in the online version at doi:10.1016/j.snb.2022.132427.

References

[1] N. Toropov, E. Osborne, L.T. Joshi, J. Davidson, C. Morgan, J. Page, J. Pepperell, F. Vollmer, SARS-CoV-2 tests: bridging the gap between laboratory sensors and clinical applications, ACS Sens 6 (2021) 2815–2837, https://doi.org/10.1021/acssensors.1c00612.

[2] P. V'kovski, A. Kratzel, S. Steiner, H. Stalder, V. Thiel, Coronavirus biology and replication: implications for SARS-CoV-2, Nat. Rev. Microbiol 19 (2021) 155–170, https://doi.org/10.1038/s41579-020-00468-6.

[3] W. Yan, Y. Zheng, X. Zeng, B. He, W. Cheng, Structural biology of SARS-CoV-2: open the door for novel therapies, Sig Transduct. Target Ther. 7 (2022) 26, https://doi.org/10.1038/s41392-022-00884-5.

[4] C.B. Jackson, M. Farzan, B. Chen, H. Choe, Mechanisms of SARS-CoV-2 entry into cells, Nat. Rev. Mol. Cell Biol. 23 (2022) 3–20, https://doi.org/10.1038/s41580-021-00418-x.

[5] J. Shang, Y. Wan, C. Luo, G. Ye, Q. Geng, A. Auerbach, F. Li, Cell entry mechanisms of SARS-CoV-2, Proc. Natl. Acad. Sci. USA 117 (2020) 11727–11734, https://doi.org/10.1073/pnas.2003138117.

[6] J. Shang, G. Ye, K. Shi, Y. Wan, C. Luo, H. Aihara, Q. Geng, A. Auerbach, F. Li, Structural basis of receptor recognition by SARS-CoV-2, Nature 581 (2020) 221–224, https://doi.org/10.1038/s41586-020-2179-y.

[7] J. Yang, S.J.L. Petitjean, M. Koehler, Q. Zhang, A.C. Dumitru, W. Chen, S. Derclaye, S.P. Vincent, P. Soumillion, D. Alsteens, Molecular interaction and inhibition of SARS-CoV-2 binding to the ACE2 receptor, Nat. Commun. 11 (2020) 4541, https://doi.org/10.1038/s41467-020-18319-6.

[8] F. Saponaro, G. Rutigliano, S. Sestito, L. Bandini, B. Storti, R. Bizzarri, R. Zucchi, ACE2 in the Era of SARS-CoV-2: Controversies and Novel Perspectives, Front. Mol. Biosci. 7 (2020), 588618, https://doi.org/10.3389/fmolb.2020.588618.

[9] I.M. Ibrahim, D.H. Abdelmalek, M.E. Elshahat, A.A. Elfiky, COVID-19 spike-host cell receptor GRP78 binding site prediction, J. Infect. 80 (2020) 554–562, https://doi.org/10.1016/j.jinf.2020.02.026.

[10] K. Wang, W. Chen, Z. Zhang, Y. Deng, J.-Q. Lian, P. Du, D. Wei, Y. Zhang, X.-X. Sun, L. Gong, X. Yang, L. He, L. Zhang, Z. Yang, J.-J. Geng, R. Chen, H. Zhang, B. Wang, Y.-M. Zhu, G. Nan, J.-L. Jiang, L. Li, J. Wu, P. Lin, W. Huang, L. Xie, Z.-H. Zheng, K. Zhang, J.-L. Miao, H.-Y. Cui, M. Huang, J. Zhang, L. Fu, X.-M. Yang, Z. Zhao, S. Sun, H. Gu, Z. Wang, C.-F. Wang, Y. Lu, Y.-Y. Liu, Q.-Y. Wang, H. Bian, P. Zhu, Z.-N. Chen, CD147-spike protein is a novel route for SARS-CoV-2 infection to host cells, Sig Transduct. Target Ther. 5 (2020) 283, https://doi.org/10.1038/s41392-020-00426-x.

[11] K.T. Iacono, A.L. Brown, M.I. Greene, S.J. Saouaf, CD147 immunoglobulin superfamily receptor function and role in pathology, Exp. Mol. Pathol. 83 (2007) 283–295, https://doi.org/10.1016/j.yexmp.2007.08.014.

[12] U. Radzikowska, M. Ding, G. Tan, D. Zhakparov, Y. Peng, P. Wawrzyniak, M. Wang, S. Li, H. Morita, C. Altunbulakli, M. Reiger, A.U. Neumann, N. Lunjani, C. Traidl-Hoffmann, K.C. Nadeau, L. O'Mahony, C. Akdis, M. Sokolowska, Distribution of ACE2, CD147, CD26, and other SARS-CoV-2 associated molecules in tissues and immune cells in health and in asthma, COPD, obesity, hypertension, and COVID-19 risk factors, Allergy 75 (2020) 2829–2845, https://doi.org/10.1111/all.14429.

[13] U. Radzikowska, M. Ding, G. Tan, D. Zhakparov, Y. Peng, P. Wawrzyniak, M. Wang, S. Li, H. Morita, C. Altunbulakli, M. Reiger, A.U. Neumann, N. Lunjani, C. Traidl-Hoffmann, K.C. Nadeau, L. O'Mahony, C. Akdis, M. Sokolowska, Distribution of ACE2, CD147, CD26, and other SARS-CoV-2 associated molecules in tissues and immune cells in health and in asthma, COPD, obesity, hypertension, and COVID-19 risk factors, Allergy 75 (2020) 2829–2845, https://doi.org/10.1111/all.14429.

[14] WHO, Methods for the detection and identification of SARS-CoV-2 variants Summary Diagnostic screening assays of known VOCs S-gene drop out or target failure, 2021. ⟨https://www.who.int/publications/i/item/diagnostic⟩.

[15] X. Ding, Z. Li, C. Liu, Monolithic, 3D-printed lab-on-disc platform for multiplexed molecular detection of SARS-CoV-2, Sens. Actuators B: Chem. 351 (2022), 130998, https://doi.org/10.1016/j.snb.2021.130998.

[16] P.-H. Chen, C.-C. Huang, C.-C. Wu, P.-H. Chen, A. Tripathi, Y.-L. Wang, Saliva-based COVID-19 detection: A rapid antigen test of SARS-CoV-2 nucleocapsid protein using an electrical-double-layer gated field-effect transistor-based biosensing system, Sens. Actuators B: Chem. 357 (2022), 131415, https://doi.org/10.1016/j.snb.2022.131415.

[17] Y.T. Büyüksünetçi, B. Ekrem Çitil, Ü. Anık, An impedimetric approach for COVID-19 detection, Analyst 147 (2022) 130–138, https://doi.org/10.1039/D1AN01718G.

[18] N. Kumar, N.P. Shetti, S. Jagannath, T.M. Aminabhavi, Electrochemical sensors for the detection of SARS-CoV-2 virus, Chem. Eng. J. 430 (2022), 132966, https://doi.org/10.1016/j.cej.2021.132966.

[19] P.K. Sharma, E.-S. Kim, S. Mishra, E. Ganbold, R.-S. Seong, A.K. Kaushik, N.-Y. Kim, Ultrasensitive and Reusable Graphene Oxide-Modified Double-Interdigitated Capacitive (DIDC) Sensing Chip for Detecting SARS-CoV-2, ACS Sens 6 (2021) 3468–3476, https://doi.org/10.1021/acssensors.1c01437.

[20] M. Adeel, K. Asif, V. Canzonieri, H.R. Barai, Md.M. Rahman, S. Daniele, F. Rizzolio, Controlled, partially exfoliated, self-supported functionalized flexible graphitic carbon foil for ultrasensitive detection of SARS-CoV-2 spike protein, Sens. Actuators B: Chem. 359 (2022), 131591, https://doi.org/10.1016/j.snb.2022.131591.

[21] I.A. Mattioli, K.R. Castro, L.J.A. Macedo, G.C. Sedenho, M.N. Oliveira, I. Todeschini, P.M. Vitale, S.C. Ferreira, E.R. Manuli, G.M. Pereira, E.C. Sabino, F. N. Crespilho, Graphene-based hybrid electrical-electrochemical point-of-care device for serologic COVID-19 diagnosis, Biosens. Bioelectron. 199 (2022), 113866, https://doi.org/10.1016/j.bios.2021.113866.

[22] R.M. Torrente-Rodríguez, H. Lukas, J. Tu, J. Min, Y. Yang, C. Xu, H.B. Rossiter, W. Gao, SARS-CoV-2 RapidPlex: A Graphene-Based Multiplexed Telemedicine Platform for Rapid and Low-Cost COVID-19 Diagnosis and Monitoring, Matter 3 (2020) 1981–1998, https://doi.org/10.1016/j.matt.2020.09.027.

[23] P. Slepski, M. Szocinski, J. Majcherczak, H. Gerengi, K. Darowicki, New Method of Non-Linear Electrochemical Impedance Spectroscopy with an Amplitude-Modulated Perturbation Signal, J. Electrochem. Soc. 166 (2019) C559–C563, https://doi.org/10.1149/2.0831915jes.

[24] K. Darowicki, P. Ślepski, Instantaneous electrochemical impedance spectroscopy of electrode reactions, Electrochim. Acta 49 (2004) 763–772, https://doi.org/10.1016/j.electacta.2003.09.030.

[25] J. Ryl, R. Bogdanowicz, P. Slepski, M. Sobaszek, K. Darowicki, Dynamic Electrochemical Impedance Spectroscopy (DEIS) as a Tool for Analyzing Surface Oxidation Processes on Boron-Doped Diamond Electrodes, J. Electrochem. Soc. 161 (2014) H359–H364, https://doi.org/10.1149/2.016406jes.

[26] W. Lipińska, J. Ryl, P. Slepski, K. Siuzdak, K. Grochowska, Exploring multi-step glucose oxidation kinetics at GOx-functionalized nanotextured gold surfaces with differential impedimetric technique, Measurement 174 (2021), 109015, https://doi.org/10.1016/j.measurement.2021.109015.

[27] P. Niedzialkowski, P. Slepski, J. Wysocka, J. Chamier-Cieminska, L. Burczyk, M. Sobaszek, A. Wcislo, T. Ossowski, R. Bogdanowicz, J. Ryl, Multisine impedimetric probing of biocatalytic reactions for label-free detection of DEFB1 gene: How to verify that your dog is not human? Sens. Actuators B: Chem. 323 (2020), 128664 https://doi.org/10.1016/j.snb.2020.128664.

[28] J. Ryl, M. Cieslik, A. Zielinski, M. Ficek, B. Dec, K. Darowicki, R. Bogdanowicz, High-temperature oxidation of heavy boron-doped diamond electrodes: microstructural and electrochemical performance modification, Materials 13 (2020) 964, https://doi.org/10.3390/ma13040964.

[29] S. Fudala-Ksiazek, M. Sobaszek, A. Luczkiewicz, A. Pieczynska, A. Ofiarska, A. Fiszka-Borzyszkowska, M. Sawczak, M. Ficek, R. Bogdanowicz, E.M. Siedlecka, Influence of the boron doping level on the electrochemical oxidation of raw landfill leachates: Advanced pre-treatment prior to the biological nitrogen removal, Chem. Eng. J. 334 (2018) 1074–1084, https://doi.org/10.1016/j.cej.2017.09.196.

[30] J. Ryl, L. Burczyk, A. Zielinski, M. Ficek, A. Franczak, R. Bogdanowicz, K. Darowicki, Heterogeneous oxidation of highly boron-doped diamond electrodes and its influence on the surface distribution of electrochemical activity, Electrochim. Acta 297 (2019) 1018–1027, https://doi.org/10.1016/j.electacta.2018.12.050.

[31] S. Phal, B. Shatri, A. Berisha, P. Geladi, B. Lindholm-Sethson, S. Tesfalidet, Covalently electrografted carboxyphenyl layers onto gold surface serving as a platform for the construction of an immunosensor for detection of methotrexate, J. Electroanal. Chem. 812 (2018) 235–243, https://doi.org/10.1016/j.jelechem.2017.12.072.

[32] Z. Salmi, A. Lamouri, P. Decorse, M. Jouini, A. Boussadi, J. Achard, A. Gicquel, S. Mahouche-Chergui, B. Carbonnier, M.M. Chehimi, Grafting polymer–protein bioconjugate to boron-doped diamond using aryl diazonium coupling agents, Diam. Relat. Mater. 40 (2013) 60–68, https://doi.org/10.1016/j.diamond.2013.10.007.

[33] Ľ. Švorc, D. Jambrec, M. Vojs, S. Barwe, J. Clausmeyer, P. Michniak, M. Marton, W. Schuhmann, Doping Level of Boron-Doped Diamond Electrodes Controls the Grafting Density of Functional Groups for DNA Assays, ACS Appl. Mater. Interfaces 7 (2015) 18949–18956, https://doi.org/10.1021/acsami.5b06394.

[34] N. Zehani, P. Fortgang, M. Saddek Lachgar, A. Baraket, M. Arab, S.V. Dzyadevych, R. Kherrat, N. Jaffrezic-Renault, Highly sensitive electrochemical biosensor for bisphenol A detection based on a diazonium-functionalized boron-doped diamond electrode modified with a multi-walled carbon nanotube-tyrosinase hybrid film, Biosens. Bioelectron. 74 (2015) 830–835, https://doi.org/10.1016/j.bios.2015.07.051.

[35] G. Liu, J. Liu, T.P. Davis, J.J. Gooding, Electrochemical impedance immunosensor based on gold nanoparticles and aryl diazonium salt functionalized gold electrodes for the detection of antibody, Biosens. Bioelectron. 26 (2011) 3660–3665, https://doi.org/10.1016/j.bios.2011.02.026.

[36] G. Liu, T. Böcking, J.J. Gooding, Diazonium salts: Stable monolayers on gold electrodes for sensing applications, J. Electroanal. Chem. 600 (2007) 335–344, https://doi.org/10.1016/j.jelechem.2006.09.012.

[37] L.-G. Zamfir, I. Geana, S. Bourigua, L. Rotariu, C. Bala, A. Errachid, N. Jaffrezic-Renault, Highly sensitive label-free immunosensor for ochratoxin A based on functionalized magnetic nanoparticles and EIS/SPR detection, Sens. Actuators B: Chem. 159 (2011) 178–184, https://doi.org/10.1016/j.snb.2011.06.069.
[38] P. Slepski, K. Darowicki, M. Kopczyk, A. Sierczynska, K. Andrearczyk, Electrochemical impedance studies of AB5-type hydrogen storage alloy, J. Power Sources 195 (2010) 2457–2462, https://doi.org/10.1016/j.jpowsour.2009.11.089.
[39] B. Hirschorn, M.E. Orazem, B. Tribollet, V. Vivier, I. Frateur, M. Musiani, Determination of effective capacitance and film thickness from constant-phase-element parameters, Electrochim. Acta 55 (2010) 6218–6227, https://doi.org/10.1016/j.electacta.2009.10.065.
[40] A. Ahmed, J.V. Rushworth, N.A. Hirst, P.A. Millner, Biosensors for Whole-Cell Bacterial Detection, Clin. Microbiol Rev. 27 (2014) 631–646, https://doi.org/10.1128/CMR.00120-13.
[41] E.B. Bahadır, M.K. Sezgintürk, Electrochemical biosensors for hormone analyses, Biosens. Bioelectron. 68 (2015) 62–71, https://doi.org/10.1016/j.bios.2014.12.054.
[42] R Core Team, R: A language and environment for statistical computing. R Foundation for Statistical Computing, 2013. ⟨http://www.R-project.org/⟩.
[43] S. Lê, J. Josse, F. Husson, FactoMineR: An R Package for Multivariate Analysis, J. Stat. Softw. 25 (2008), https://doi.org/10.18637/jss.v025.i01.
[44] S. Kucheryavskiy, mdatools – R package for chemometrics, Chemom. Intell. Lab. Syst. 198 (2020), 103937, https://doi.org/10.1016/j.chemolab.2020.103937.
[45] Andri et mult. al., DescTools: Tools for Descriptive Statistics, 2021. ⟨https://cran.r-project.org/package=DescTools⟩.
[46] R. Yan, Y. Zhang, Y. Li, L. Xia, Y. Guo, Q. Zhou, Structural basis for the recognition of SARS-CoV-2 by full-length human ACE2, Science 367 (2020) 1444–1448, https://doi.org/10.1126/science.abb2762.
[47] S. Osella, M. Kiliszek, E. Harputlu, C.G. Unlu, K. Ocakoglu, B. Trzaskowski, J. Kargul, Role of metal centers in tuning the electronic properties of graphene-based conductive interfaces, J. Phys. Chem. C. 123 (2019) 8623–8632, https://doi.org/10.1021/acs.jpcc.9b00170.
[48] M. Baek, F. DiMaio, I. Anishchenko, J. Dauparas, S. Ovchinnikov, G.R. Lee, J. Wang, Q. Cong, L.N. Kinch, R.D. Schaeffer, C. Millán, H. Park, C. Adams, C. R. Glassman, A. DeGiovanni, J.H. Pereira, A.V. Rodrigues, A.A. van Dijk, A. C. Ebrecht, D.J. Opperman, T. Sagmeister, C. Buhlheller, T. Pavkov-Keller, M. K. Rathinaswamy, U. Dalwadi, C.K. Yip, J.E. Burke, K.C. Garcia, N.V. Grishin, P. D. Adams, R.J. Read, D. Baker, Accurate prediction of protein structures and interactions using a three-track neural network, Science 373 (2021) 871–876, https://doi.org/10.1126/science.abj8754.
[49] J. Huang, A.D. MacKerell, CHARMM36 all-atom additive protein force field: Validation based on comparison to NMR data, J. Comput. Chem. 34 (2013) 2135–2145, https://doi.org/10.1002/jcc.23354.
[50] M.J. Abraham, T. Murtola, R. Schulz, S. Páll, J.C. Smith, B. Hess, E. Lindahl, GROMACS: High performance molecular simulations through multi-level parallelism from laptops to supercomputers, SoftwareX 1–2 (2015) 19–25, https://doi.org/10.1016/j.softx.2015.06.001.
[51] M. Tarini, P. Cignoni, C. Montani, Ambient Occlusion and Edge Cueing for Enhancing Real Time Molecular Visualization, IEEE Trans. Vis. Comput. Graph. 12 (2006) 1237–1244, https://doi.org/10.1109/TVCG.2006.115.
[52] G.C.P. van Zundert, J.P.G.L.M. Rodrigues, M. Trellet, C. Schmitz, P.L. Kastritis, E. Karaca, A.S.J. Melquiond, M. van Dijk, S.J. de Vries, A.M.J.J. Bonvin, The HADDOCK2.2 Web Server: User-Friendly Integrative Modeling of Biomolecular Complexes, J. Mol. Biol. 428 (2016) 720–725, https://doi.org/10.1016/j.jmb.2015.09.014.
[53] M.A. Helal, S. Shouman, A. Abdelwaly, A.O. Elmehrath, M. Essawy, S.M. Sayed, A. H. Saleh, N. El-Badri, Molecular basis of the potential interaction of SARS-CoV-2 spike protein to CD147 in COVID-19 associated-lymphopenia, J. Biomol. Struct. Dyn. 40 (2022) 1109–1119, https://doi.org/10.1080/07391102.2020.1822208.
[54] M.J. Glowacki, M. Cieslik, M. Sawczak, A. Koterwa, I. Kaczmarzyk, R. Jendrzejewski, L. Szynkiewicz, T. Ossowski, R. Bogdanowicz, P. Niedzialkowski, J. Ryl, Helium-assisted, solvent-free electro-activation of 3D printed conductive carbon-polylactide electrodes by pulsed laser ablation, Appl. Surf. Sci. 556 (2021), 149788, https://doi.org/10.1016/j.apsusc.2021.149788.
[55] J. Ryl, J. Wysocka, M. Cieslik, H. Gerengi, T. Ossowski, S. Krakowiak, P. Niedzialkowski, Understanding the origin of high corrosion inhibition efficiency of bee products towards aluminium alloys in alkaline environments, Electrochim. Acta 304 (2019) 263–274, https://doi.org/10.1016/j.electacta.2019.03.012.
[56] T. Siudyga, M. Kapkowski, D. Janas, T. Wasiak, R. Sitko, M. Zubko, J. Szade, K. Balin, J. Klimontko, D. Lach, J. Popiel, A. Smoliński, J. Polanski, Nano-Ru Supported on Ni Nanowires for Low-Temperature Carbon Dioxide Methanation, Catalysts 10 (2020) 513, https://doi.org/10.3390/catal10050513.
[57] P. Niedziałkowski, R. Bogdanowicz, P. Zięba, J. Wysocka, J. Ryl, M. Sobaszek, T. Ossowski, Melamine-modified boron-doped diamond towards enhanced detection of adenine, guanine and caffeine, Electroanalysis 28 (2016) 211–221, https://doi.org/10.1002/elan.201500528.
[58] S.R. Chinnadayyala, S. Cho, Electrochemical Immunosensor for the Early Detection of Rheumatoid Arthritis Biomarker: Anti-Cyclic Citrullinated Peptide Antibody in Human Serum Based on Avidin-Biotin System, Sensors 21 (2020) 124, https://doi.org/10.3390/s21010124.
[59] L. Liu, D. Deng, Y. Xing, S. Li, B. Yuan, J. Chen, N. Xia, Activity analysis of the carbodiimide-mediated amine coupling reaction on self-assembled monolayers by cyclic voltammetry, Electrochim. Acta 89 (2013) 616–622, https://doi.org/10.1016/j.electacta.2012.11.049.
[60] T.-C. Tsai, C.-W. Liu, Y.-C. Wu, N.A.P. Ondevilla, M. Osawa, H.-C. Chang, In situ study of EDC/NHS immobilization on gold surface based on attenuated total reflection surface-enhanced infrared absorption spectroscopy (ATR-SEIRAS, Colloids Surf. B: Biointerfaces 175 (2019) 300–305, https://doi.org/10.1016/j.colsurfb.2018.12.009.
[61] Q. Zhang, R. Xiang, S. Huo, Y. Zhou, S. Jiang, Q. Wang, F. Yu, Molecular mechanism of interaction between SARS-CoV-2 and host cells and interventional therapy, Sig Transduct. Target Ther. 6 (2021) 1–19, https://doi.org/10.1038/s41392-021-00653-w.
[62] R.A. Latour, The langmuir isotherm: A commonly applied but misleading approach for the analysis of protein adsorption behavior: Protein Adsorption and the Langmuir Isotherm, J. Biomed. Mater. Res. 103 (2015) 949–958, https://doi.org/10.1002/jbm.a.35235.
[63] K. Nakanishi, T. Sakiyama, K. Imamura, On the adsorption of proteins on solid surfaces, a common but very complicated phenomenon, J. Biosci. Bioeng. 91 (2001) 233–244, https://doi.org/10.1016/S1389-1723(01)80127-4.
[64] S.M. Moosavi, S. Ghassabian, Linearity of Calibration Curves for Analytical Methods: A Review of Criteria for Assessment of Method Reliability, in: M. T. Stauffer (Ed.), Calibration and Validation of Analytical Methods - A Sampling of Current Approaches, InTech, 2018, https://doi.org/10.5772/intechopen.72932.
[65] A. Gosai, X. Ma, G. Balasubramanian, P. Shrotriya, Electrical Stimulus Controlled Binding/Unbinding of Human Thrombin-Aptamer Complex, Sci. Rep. 6 (2016) 37449, https://doi.org/10.1038/srep37449.
[66] R. Cataldo, M. Leuzzi, E. Alfinito, Modelling and development of electrical aptasensors: a short review, Chemosensors 6 (2018) 20, https://doi.org/10.3390/chemosensors6020020.
[67] M. Jacquet, S. Osella, E. Harputlu, B. Pałys, M. Kaczmarek, E.K. Nawrocka, A. A. Rajkiewicz, M. Kalek, P.P. Michałowski, B. Trzaskowski, C.G. Unlu, W. Lisowski, M. Pisarek, K. Kazimierczuk, K. Ocakoglu, A. Więckowska, J. Kargul, Diazonium-based covalent molecular wiring of single-layer graphene leads to enhanced unidirectional photocurrent generation through the p-doping effect, Chem. Mater. 34 (2022) 3744–3758, https://doi.org/10.1021/acs.chemmater.2c00088.
[68] M. Jacquet, M. Izzo, S. Osella, S. Kozdra, P.P. Michałowski, D. Gołowicz, K. Kazimierczuk, M.T. Gorzkowski, A. Lewera, M. Teodorczyk, B. Trzaskowski, R. Jurczakowski, D.T. Gryko, J. Kargul, Development of a universal conductive platform for anchoring photo- and electroactive proteins using organometallic terpyridine molecular wires, Nanoscale 13 (2021) 9773–9787, https://doi.org/10.1039/D0NR08870F.
[69] C. Xu, Y. Wang, C. Liu, C. Zhang, W. Han, X. Hong, Y. Wang, Q. Hong, S. Wang, Q. Zhao, Y. Wang, Y. Yang, K. Chen, W. Zheng, L. Kong, F. Wang, Q. Zuo, Z. Huang, Y. Cong, Conformational dynamics of SARS-CoV-2 trimeric spike glycoprotein in complex with receptor ACE2 revealed by cryo-EM, Sci. Adv. 7 (2021) eabe5575, https://doi.org/10.1126/sciadv.abe5575.
[70] C.R. Arbeitman, P. Rojas, P. Ojeda-May, M.E. Garcia, The SARS-CoV-2 spike protein is vulnerable to moderate electric fields, Nat. Commun. 12 (2021) 5407, https://doi.org/10.1038/s41467-021-25478-7.
[71] M. Tagliazucchi, Y. Rabin, I. Szleifer, Ion Transport and Molecular Organization Are Coupled in Polyelectrolyte-Modified Nanopores, J. Am. Chem. Soc. 133 (2011) 17753–17763, https://doi.org/10.1021/ja2063605.
[72] S. Devarakonda, S. Kim, B. Ganapathysubramanian, P. Shrotriya, Designing asymmetrically modified nanochannel sensors using virtual EIS, Electrochim. Acta 403 (2022), 139694, https://doi.org/10.1016/j.electacta.2021.139694.
[73] A. Gosai, B.S. Hau Yeah, M. Nilsen-Hamilton, P. Shrotriya, Label free thrombin detection in presence of high concentration of albumin using an aptamer-functionalized nanoporous membrane, Biosens. Bioelectron. 126 (2019) 88–95, https://doi.org/10.1016/j.bios.2018.10.010.
[74] A. Georgas, E. Lampas, D.P. Houhoula, A. Skoufias, S. Patsilinakos, I. Tsafaridis, G. P. Patrinos, N. Adamopoulos, A. Ferraro, E. Hristoforou, ACE2-based capacitance sensor for rapid native SARS-CoV-2 detection in biological fluids and its correlation with real-time PCR, Biosens. Bioelectron. 202 (2022), 114021, https://doi.org/10.1016/j.bios.2022.114021.
[75] B. Mattiasson, M. Hedström, Capacitive biosensors for ultra-sensitive assays, TrAC Trends Anal. Chem. 79 (2016) 233–238, https://doi.org/10.1016/j.trac.2015.10.016.
[76] J. Sopoušek, J. Věžník, J. Houser, P. Skládal, K. Lacina, Crucial factors governing the electrochemical impedance on protein-modified surfaces, Electrochim. Acta 388 (2021), 138616, https://doi.org/10.1016/j.electacta.2021.138616.
[77] E. von Witting, S. Hober, S. Kanje, Affinity-based methods for site-specific conjugation of antibodies, Bioconjugate Chem. 32 (2021) 1515–1524, https://doi.org/10.1021/acs.bioconjchem.1c00313.
[78] M. Yuan, H. Liu, N.C. Wu, I.A. Wilson, Recognition of the SARS-CoV-2 receptor binding domain by neutralizing antibodies, Biochem. Biophys. Res. Commun. 538 (2021) 192–203, https://doi.org/10.1016/j.bbrc.2020.10.012.
[79] D. Prozeller, C. Rosenauer, S. Morsbach, K. Landfester, Immunoglobulins on the surface of differently charged polymer nanoparticles, Biointerphases 15 (2020), 031009, https://doi.org/10.1116/6.0000139.

Mateusz Brodowski received his engineer degree in 2019 at the of Chemical Technology with a specialization in AntiCorrosion Protection Technologies, in his engineer thesis he examined the effectiveness of green corrosion inhibitors. He finished a Master's degree in the field of Mechatronics, realizing the work of creating software for data acquisition from the electrochemical measurement system. Since 2021 he is a Ph.D. student at Gdańsk University of Technology. From 2019–2021, he has been working as a Chemist at the Institute of Biotechnology and Molecular Medicine in the electrochemistry department.

Mattia Pierpaoli main interests and competencies lie in the field of advanced carbon nanomaterials for environmental applications and sensing. In 2019 he was awarded the

PhD title, after being visiting PhD student at the Gdansk University of Technology (Poland) and Shanghai Jiao Tong University (China). He is currently conducting research on novel CVD-grown three-dimensional carbon nanomaterials at the Gdańsk University of Technology.

Monika Janik received the B.Sc. and M.Sc. degrees in biotechnology from the Wroclaw University of Science and Technology, Poland, in 2014 and 2015, respectively. In 2019 she received a Ph.D. degree in photonics from the Université du Québec en Outaouais, Canada. Since August 2019, she has been an Assistant Professor at the Institute of Microelectronics and Optoelectronics, Warsaw University of Technology. Moreover, since December 2019, she has been a postdoctoral fellow at the Department of Metrology and Optoelectronics, Gdańsk University of Technology. Her current interests include designing and optimizing different kinds of biosensors.

Marcin Kowalski received his engineer degree in 2019 at the of Chemical Technology with a specialization in Anti-Corrosion Protection Technologies - Gdansk University of Technology. He continued his Master's degree studies at the Faculty of Mechanical Engineering - Mechatronics, which he completed in 2021. From 2019–2022, he has been working as a scientist at the Diamondized Electronics Group, where he dealt with the functionalization of the diamond surface for sensory purposes. Additionally, he took an active part in creating software for electrochemical data acquisition. Currently, he works as a chemist at the Institute of Biotechnology and Molecular Medicine. He mainly works with electrochemical measurements of ultra-sensitive electrodes, modified with biological molecules.

Mateusz Ficek was born in Gdansk in 1988. He received his Ph.D. degree with honours in Electronics from the Gdansk University of Technology in 2019. Currently he is an Assistant Professor at the Faculty of Electronics at Gdansk University of Technology. His current domains of interest include selective CVD diamond growth and nanocrystalline diamond doping for environmental and biochemical nanosensors.

Paweł Ślepski (orcid.org/0000–0001–7856–3098) received his Ph.D. in Chemical Technology in 2005, habilitation in 2015. Since 2018 he works as Associate Professor at Gdansk University of Technology, Poland, in the Department of Electrochemistry, Corrosion and Materials Engineering. His scientific areas of activity are related with electrochemistry, materials engineering and corrosion processes, in particular application of impedance spectroscopy to study nonstationary and nonlinear systems. Dr. Ślepski is co-author of over 40 articles related to electrochemistry (h-index 19).

Bartosz Trzaskowski (born 1977) received his Ph.D. in Chemistry from the University of Warsaw in 2005. He worked as a post-doc researcher at the University of Arizona and California Institute of Technology. He moved back to the University of Warsaw in 2010 and from 2013 he is the head of Chemical and Biological Systems Simulation Laboratory at the Centre of New Technologies. His main research area is the mechanistic description of various catalytic processes, particularly those related to olefin metathesis catalyzed by ruthenium-based complexes. He is also interested in chemistry of carbenes, organocatalysis and mechanically interlocked molecular architectures in the context of stereoselective catalysis as well as in multi-scale computational description of chemical and biological phenomena.

Greg M. Swain is a Professor in the Department of Chemistry, Michigan State University. His group's current research is at the crossroads of carbon materials science and physical and analytical electrochemistry. The current projects include diamond and diamond-like carbon electrodes for electroanalysis, optically transparent diamond electrodes for spectroelectrochemistry, nanocarbon powders as advanced materials for separations, and diamond microelectrodes for neuroanalytical chemistry and chemical and biochemical sensors. He previously served as Editor and Editor-in-Chief of Diamond and Related Materials (Elsevier) (2011–2015) and he currently serves on the advisory board of Advanced Engineering Materials (Wiley).

Jacek Ryl (born 1982) is an Associate Professor and Head of the Division of Electrochemistry and Surface Physical Chemistry at the Institute of Nanotechnology and Materials Engineering, Gdansk University of Technology. He has received a Ph.D. (2010) and habilitation (2018) in Chemical Technology at GUT. The principal area of scientific activity lies in applied electrochemistry, in particular corrosion science, electrochemical sensors, electrocatalysis and wastewater treatment. He is involved in the development of instantaneous impedance techniques with multisine perturbation, dedicated to the assessment of non-stationary processes. He is co-author of over 150 peer-reviewed papers in JCR journals (h-index = 26). He was the PI (5 times) and WP leader (3 times) of projects awarded by international and national funding agencies. The most notable awards include scientific scholarship by the Minister of Science and Higher Education of Poland (2017) and the IV Division (Engineering Sciences) of the Polish Academy of Sciences award for scientific achievements (2019). Currently, he serves on the Editorial Board for 2 JCR journals, and reviewer for over 45 journals and granting agencies.

Robert Bogdanowicz (born 1976) received his Ph.D. degree with honours in Electronics from the Gdansk University of Technology in 2009. He worked as a post-doc researcher in Ernst-MoritzArndt-Universität Greifswald Institut für Physik in 2010 and 2011. He moved back to the Gdansk University of Technology in 2011, as an assistant professor in the Department of Metrology and Optoelectronics. His current domains of interest include selective CVD diamond growth and nanocrystalline diamond doping for environmental and biochemical nanosensors. In 2015 he held a scholarship Fulbright Senior Scholar Program at the California Institute of Technology (Caltech) in the group of prof. William Goddard (Materials and Process Simulation Center) working on hybrid 3D diamond structures. Prof. Bogdanowicz has published more than 100 scientific papers and book chapters, proceedings, and special journal issues (e.g., Diamond and Related Materials). He has served on several journal editorial boards and currently serves as an Associate Editor for 2 JCR journals, and reviewer for over 30 journals and granting agencies